NEAR AND MID INFRARED DEVICES FOR DEEP MEDIA SENSING AND DETECTION

A Dissertation

Presented to the Faculty of the Graduate School

of Cornell University

In Partial Fulfillment of the Requirements for the Degree of

Doctor of Philosophy

by

Romy Michelle Fain

August 2017

NEAR AND MID INFRARED DEVICES

FOR DEEP MEDIA SENSING AND DETECTION

Romy Michelle Fain, Ph. D.

Cornell University 2017

This thesis provides components for a minimally invasive mid-infrared light-delivery, sensing and detection system in silicon. Both Photonic Needles for deep-media light delivery and a CMOS-compatible waveguide-integrated detector at 3.7μm are explored in depth. Other integratable elements presented include ring resonators in the mid-infrared for gas absorption sensing and frequency comb generation, a MEMS weak electric field sensor, and wavelength sensitive gratings for directional coupling to/from the environment.

Chapter 1 provides a primer for mechanical, optical, and electrical concepts related to the work later presented in this text. The mechanical primer covers Euler bucking theory as well as an intuitive perspective on stiffness, elastic modulus, second moment of inertia, and beam bending. The optical primer covers Snell's law, ring resonators, Fresnel equations, Fabry-Perot resonances and losses, distributed Bragg reflectors, Bragg gratings, and optical coupling losses. The electrical primer covers the Fourier transform of a pulse train, noise equivalent power, loss due to impedance mismatch, and RC limited bandwidth.

In Chapter 2 we demonstrate a new platform for minimally invasive, light-delivery probes leveraging the maturing field of silicon photonics, enabling massively parallel fabrication of photonic structures. These Photonic Needles probes have sub-10μm

cross-sectional dimensions, lengths greater than 3mm-- surpassing 1000 to 1 aspect ratio, and are released completely into air without a substrate below. We show the Photonic Needles to be mechanically robust when inserted into 2% agarose. The propagation loss of these waveguides is low-- on the order of 4dB/cm.

In Chapter 3 we demonstrate a CMOS-compatible mid-infrared detector at wavelengths ranging from 3.36 to 3.74μm by exciting mid bandgap states in a sulfur-doped silicon waveguide with responsivities up to 30mA/W. We also measure a noise equivalent power (NEP) of 3e-10W/√Hz at 3.7μm wavelength and 30V reverse bias voltage.

Chapter 4 presents other device elements that could also be integrated into this same silicon on insulator (SOI) platform for long wavelengths with preliminary and/or simulation results for each. These elements could be implemented as part of future projects. Chapter 5 provides veins of promising future research directly related to the work from Chapters 2 and 3.

BIOGRAPHICAL SKETCH

Romy Fain feels her life has contradicted many of the stereotypes of women, primarily due to her mother's influence. Although her mother didn't have the same educational opportunities, she's a born engineer and renaissance woman who can build or fix anything. From the beginning, she taught Romy about art, science, cuisine, trigonometry, painting, music, costume design and anything else they were both passionate about. Most of all, she taught Romy the love of learning, and the notion that with hard work and determination, she could learn or do anything.

At seventeen, Romy moved to San Francisco and worked as a bicycle mechanic to pay for art classes. Her interest in mechanics led to an apprenticeship with a machinist, which sparked a strong interest in metallurgy and materials. This profound interest, combined with her creative drive, led her to become an accomplished metal fabricator and artist. For a decade she ran her own metal fabrication business, providing metal fabrication and design services. She particularly enjoyed engineering innovative solutions to unique problems for her clients. She also taught classes in welding, blacksmithing, and machine design. Her passion and inspiration led several of her students to go on to successful careers as renowned metal and kinetic artists. Throughout this work, she often found herself in the position of solving challenging engineering problems, and longed to pursue an in-depth engineering education.

Later, she worked in robotics research and development for Dr. David Hanson at Human Evolution Robotics. She designed several micro actuators, and built several prototypes of these, complete with closed-loop electronics. She also worked on several

designs using electro-active polymers as artificial muscles. It was here that she found that her aptitude and interests were suited to electrical as well as mechanical projects.

During this time, Romy was also active in the bay area arts community. She toured with musical groups, designed and built trick bikes for the bicycle rodeo, engineered a pneumatic valve system for fire cannons that shot flames over 100 feet in the air at the Burningman arts festival, and performed many different acts, including 'strong woman', for not one, but two circuses.

Then one day while Romy was welding an I-beam structure for a friend's new house, the scaffolding collapsed. She fell three stories to the ground, breaking her neck. Although extremely fortunate to have avoided paralysis or worse, she was told she would experience pain and reduced mobility for the rest of her life.

Determined to move ahead purposefully after the accident, Romy enrolled in her local community college as soon as she was able, to pursue her long-held dream of studying engineering. While there, she spearheaded a student research program, researching carbon nanotube-based electroactive polymers. This research produced original results not previously published. From then on, she was hooked on research. She decided she would become an engineering professor and researcher.

Her hard work and determination at community college paid off, and she was accepted to University of California, Berkeley in the Mechanical Engineering department. While an undergraduate at Berkeley, Romy worked in three different research labs, for Professor Lisa Pruitt, Professor Albert Pisano, and Professor Paul K. Wright.

Her interest in materials science led her to the Pruitt lab, where she assisted with a fatigue and micro structure study on ultra high molecular weight polyethylene

(UHMWPE), the development of an automated wear testing system for pin-on-disc testing of UHMWPE, and several studies on bioimplant retrievals, including scanning electron microscopy of occlusions on their surfaces. These studies found a fatal flaw in the microstructure of an implant that saved this design from going into large-scale production.

Concurrently, in the Pisano lab, driven to learn more about micro electromechanical systems (MEMS), Romy assisted with research on micro implantable polymer pH sensors, and a novel micro electromagnetic energy harvester. She initiated a project of her own design, an electronics case that generates power using MEMS piezoelectric bimorphs. She was issued a patent on the case, and entertained Nokia's pursuit of this technology.

Next, Romy joined the Wright lab to work on their piezoelectric energy harvesting projects and to continue her project in collaboration with the Pisano lab. She worked on a Siemens sponsored project developing new methods to study fatigue in PZT energy harvesters. She also applied an idea from multi-axis microstrain accelerometers to make 3-axis energy harvesters, which could produce significantly more power than typical single axis energy harvesters. This and other work resulted in multiple papers, including some first author and third author for the 2009 IEEE PowerMEMS Conference, as well as a journal paper in Smart Materials. She gave multiple talks and presentations to groups including the Berkeley Energy Resources Collaborative, energy advisers to President Obama, and the California Energy Commission.

Romy's work at Berkeley, and her focused concentration on micro devices led her to believe that the greatest advances could be made by controlling material structure at the

nano scale. After seeing a demonstration of optical tweezing, she became enthralled with nanophotonics and how it might be used to build new materials from the bottom up, as well as whole new worlds of applications.

Romy's interest in nanophotonics and its applications led her first to building microstructures via optical tweezing with Professor David Erickson in the Mechanical Engineering department at Cornell University. While at Cornell, and while she first began learning about the field of photonics, she also learned about the impressive body of work in photonics from Professor Michal Lipson's group. Her desire to learn more about photonics, optics and light in general, prompted her to make the move to Electrical Engineering under Michal's guidance. Professor Lipson is a powerhouse and undeniably inspiring leader in the field of silicon nanophotonics, and has given Romy this opportunity to become a valuable contributor to the field in her own right. Romy is eternally grateful for the rare opportunity she has had to contribute to Michal's significant and impactful body of work while completing her PhD at Cornell and Columbia Universities.

Romy's current research pursuits are part of her life-long quest to master a range of studies, building a knowledge base that is greater than the sum of its parts. She intends, as her next step, to use her expertise as an academic researcher and educator, inspiring the next generation with her passion for science, engineering, and empowering other non-traditional students as they pursue careers in STEM fields.

To all those brave and hearty souls out there who irreverently keep doing the “impossible”

(Keep at it! The world needs you!)

Also to Momma and to Rich
the ‘natural engineers’ in my life

ACKNOWLEDGMENTS

Thank you, to my advisor Michal Lipson for giving me the opportunity to be a part of this incredible group. I have learned so much from you and from this group that you have built from nothing. It has been the experience of a lifetime and will forever be a part of me. Thank you also for the inspiration you are, not just to me and to our group, but to the entire community. Everywhere I go people (especially women) tell me enthusiastically how inspired they are by you and the work that you do. Thank you for the amazing powerhouse that you are in the field. You have done this despite the odds, and I am sure in the face of a lot of opposition along the way. Thank you for being unstoppable.

A big thank you to the other members of my committee, Clif Pollack and Harold Craighead. You both embody both rare and unique combinations of traits. You both have unparalled expertise in your respective fields, and yet still find the time and energy to provide generous and unwavering support of your students. Clif, nobody knows more about lasers than you, but you still always have time for questions from students. I always felt like I could come and talk to you about my ideas. You have an amazing way of constructively challenging ideas, with the underlying humor, warmth and enthusiastic support you are so well known for. (Also thank you for making the ECE graduation ceremonies entertaining.) To Harold, thank you for introducing me the unique crossover of physics and biology that you invented. Your achievements are awe inspiring, and yet you always had time to talk to me about my research. Also the CNF is the amazing facility it is in large part due to your leadership. Thank you from all of us whose work has been a consequence of access to this resource.

Next I would like to thank two people who were integral to the functioning of our labgroup, the success of my research personally, Jaime Cardenas and Carl Poitras. Jaime, the depth and breadth of your knowledge about nanofabrication, not to mention optics, is stunning and has significantly contributed to probably every project coming through our labgroup while you were there. Moving on to your tenure-track position at Rochester hasn't stopped you from continuing to be a vast resource to everyone in the Lipson group. Thank you for helping me with my own job search. Your perspective on negotiating and startup requests has been especially valuable. Thank you. Carl, you can do it all-- from seamlessly keeping the lab running, to deep discussions about the nitty-gritty of physics, to developing cutting edge science—all while maintaining your outrageously hilarious sense of humor and having fun with it all. Thanks for making me crackup when I was supposed to be quietly attentive. Thanks for all of your input on my work in the group when you were there, and thank you for your excellent input on my applications. Thank you for being my friend.

To the administrative staff for our group, past and present, we could not do what we do without you. Kim, your support for the group was essential, both before and as we entered an especially chaotic time with the group moving to Columbia University. Thank you. Krystal, you are amazing. Thank you for all that you do for the group-- and always with a smile and a great attitude! You make it look easy. We know it is not. Thank you.

Both before and after I joined the Electrical and Computer Engineering department, there were a number of people in the Mechanical and Aerospace Engineering

department who selflessly provided support above and beyond the call of duty. David Erickson, thank you for all of your guidance towards winning the NSF graduate fellowship. You made all the difference. Also thank you for believing in me and my ideas, and especially for your generous support for my move to work with Michal in ECE. Ephrahim Garcia, I regret not having taken advantage of all of the mentorship and expertise you had to offer before it was too late. I'm grateful for our talks on piezoelectric energy harvesting, and nanoscale mechanics—but especially honored by your respect and generous mentorship. You are missed by many. Brian Kirby, I can always count on you for straight talk and great perspective. Thank you for all the valuable advice on both graduate school and what's next. You are an invaluable source of information about this sometimes impenetrable cloud we call Academia. Marcia Sawyer the department could not run without you, but more than that, you are always there to go the extra mile for students (and I'm guessing for faculty too). Even without having the status and influence of being department faculty behind you, you contribute more significantly toward making MAE welcoming, warm and down-to-earth than any other single member of the department. Thank you. You are essential. Alan Zehnder, thank you for your personal mentorship and support in difficult times early on, but also thank you for your support and mentorship of all the non-traditional and under-represented groups in engineering. Your work is important and does not go unrecognized.

Which brings me to Sara Hernandez—you are a powerhouse for equity and inclusion, and you do it with limitless style and grace. You deserve your own paragraph because you in a league of your own. Thank you for your service to so many communities.

To the CNF staff, you guys are a bastion of enlightened mentorship and unparalleled knowledge on nanofabrication. A cleanroom is just one big machine with a bunch of smaller machines in it. An essential part of keeping the machine running smoothly is you. (By the way, I frequently proselytize about this and the CNF specifically. Your excellence is known in the world.) Chris Alpha, whether it is expertise about fab processes, "emergency" repairs of equipment when I was on a deadline, or just listening to me kvetch about how things are not going my way, you are my go to guy at the CNF. You make things happen. You are a rare gem. Another rare gem--Mike Skvarla-- I'm sure that I owe you dozens of chocolate chip cookies at this point. You are responsible for a significant part of what is the culture of the CNF. With your nutty sense of humor, coupled with no nonsense expertise on all things nanofab, you are extraordinary. Thanks for not being the standard issue. Meridith Metzler, before the CNF lost you to Penn, you taught me a lot about etchers and helped me understand what was going wrong with my particular devices—invaluable. Gary Bordonaro, thank you for all of your help working out issues with my photoresists and ASML processes. You have also always been a reasonable and yet firm force for safety in the cleanroom, and it is appreciated. My neighbor, Alan Bleier, not only are you a source of unshakable calm and expertise in the cleanroom, but you have inspired me and I'm sure others with your relentless summiting of West Hill everyday on your bicycle. John Grazul, eventhough you are officially CCMR and not CNF, I still relate you to the same culture of excellence and impeccable attitudes. Thank you for your "anything goes" attitude (within safety constraints, of course). Your lab, like your personality, is totally unique. In a few square feet of brilliantly organized miscellanea, you somehow fill countless holes in

what we as researchers need to make our projects reality. So cool. Plus as a bonus you are always a joy to work with. Thank you.

This paragraph is for the unofficial CNF staff members (e.g. former Tornado folks) to whom I am also indebted. To Chris Martin, you were always there to help trouble shoot processes, offer great solutions and generally be a fun person to kill time with while waiting for that etch to finish. To Nick Sherwood, you and Erin helped me get through some rough times, both in and out of the cleanroom. Thanks for believing in me, thanks for the pep talks, thanks lending me your fab and SEM expertise, and especially thanks for making me dinner when I had to work late.

To the staff at the Advanced Science Research Center (ASRC) at City University of New York (CUNY), I haven't had as much time with you guys since most of my fabrication for my PhD was complete before our move to Columbia University. But you have all been very helpful in my short time there-- even with your hands full getting a world-class cleanroom facility off the ground and added stress from all of us at Columbia straining your resources while the Columbia cleanroom has been in construction. Especially thanks to Jacob Travino. You have been extraordinarily patient, accommodating and responsive to our group's needs. (Sorry about that dicing saw blade.) Thank you for your leadership. Also thank you to Milan, Shawn and Vishal for keeping the cleanroom running smoothly and personally helping me with new recipes for depositions and figuring out how to get good absorption measurements on the ellipsometer (just to name a couple of examples). I hope we have a chance to work together in the future.

To my “shipmates,” I will never forget you. Everyone in our research group, without exception, is extraordinary, as scientists and engineers and especially as positive generous, human beings. I owe a great deal of my current success to you. I am so proud to be your colleague, and I hope you know that I am still here for you if you need me, or if you just want to talk ideas! Aseema Mohanty, starting with those initial conversations at SWE events and before I had even joined the group, you have been such a friend to me, in thick and thin. So many times you were really the only person who understood. Thank you. Thanks for all those awesome dinners and kvetch-fests. You get it. Also thank you for always being available as a great sounding board for research ideas and solving problems. Don’t forget you are destined for greatness. Kevin Luke, what a joy it was to get to work with you while you were in the group. Thank you for having so many down-to-earth explanations for concepts that had eluded me previously. I’m glad you are enjoying your life as a globe trotter, and I’m glad to call you my friend. Steven Miller, thanks for helping me push over those initial results for the detectors. Your knowledge and experience in the mid-IR has been a huge benefit to my work and I am sure will be to the next generation as well. Thanks for lending me your long arms (and smarts and time and…) to align all those hard to reach optics. Also thanks for all the music and the BBQs and the friendship. Chris Phare, you are a such a wealth of knowledge on so many topics. Thank you for sharing it on so many occasions, and thank you for just being there to listen and help me process ideas. Avik Dutt, thank you for all the terrible puns! But especially thank you for always being an enthusiastic participant in converations about science. Your unassuming yet deep understanding of physics is a gift to us all. Academia is lucky to have you. Austin Griffith, we so much

miss the grand gestures and preposterous adjectives! Thanks for explaining your approximation for coupling from a quantum mechanics perspective. So helpful! And thanks for just generally being so open and affable when broaching so many subjects, from Physics to Nanofab to Coffee. Shreyas Shah, my neighbor in the office before we moved, thanks for the chats about detectors, and thanks for lending me your coffee cup on more than one occasion. It was fun trying to tango with you. You deserve all the best. Mian Zhang, thanks for being open to new ideas and thanks for sharing so many of yours. Its great to see you thriving in academia. Lawrence Tzuang and Yoon Ho Daniel Lee, you guys both got me started on the right track with the active fabrication runs. Thanks for all of your selfless input, even while you guys were almost out the door. Felippe Barbosa, what an inspiring combination of tireless work ethic, depth of knowledge about physics, and just being a pleasure to work with. I am so glad that I had all your input on the in vivo experiments with the photonic needles. You really were all in. Thank you. Amin thank you for your always humble and kind contributions to all of our neural work. Your RainX method saved the day. Raph! (Raphael) I am so glad I got to know you, and your beautiful family, while you were in the group. Thank you for your right-on-point input with the DBR and absorption experiments. I'll try to stop scaring your children with the robots in the future. Bishu Guha, I always loved the ideas you came up with—especially the thermal projects. Thank you for sharing them with us. Gaurang Bhatt, thank you for putting in a valiant effort to help solve some of the outstanding mysteries surrounding the detectors. (No really, thank you for your input!) I really hope we get to work on some thermal applications for these in the future. Ipshita Datta, thank you for being so forthcoming and gregarious (in other words, LOUD!).

Seriously though, it is such a joy to see a woman fearlessly speak up for herself. Bonus: you have the smarts to back it up. Thank you for your friendship. Brian Stern thank you for all the hilarious, and thoroughly understated, jokes. Oscar A Jimenez Gordillo thank you for your endlessly kind spirit and always making things a little brighter. Xingchen (William) Ji, thank you for taking on all the nitride fab for everyone. I know it is a thankless job—so thank you. And thanks for the awesome hot pot. Brian Lee, thank you for your no-nonsense, get-things-done attitude. You help keep the apathy in the lab to a minimum. Moshe Zadka, thank you for keeping all of the servers running and always responding quickly to my questions about them and the software and…. You-Chia Chang, you haven't been in the group long, but since you have been my neighbor in the office, I have seen enough to know that the depth of your knowledge on optics is great. Thank you for the quality, if not quantity, of spot-on conversations. Tong Lin, Utsav D Dave, and Goran Kovacevic you guys I never had a chance to spend a lot of time getting to know, but I really enjoyed the conversations we did have. Samantha Roberts, luckily I started getting to know you before you came to the group, from the CNF at Cornell. Thank you for so generously sharing all of your hard-won fabrication expertise, with the group and with me in particular. And thanks for the wine and pasta when it all seemed to be getting overwhelming.

To all at LNG, I sincerely hope we have the opportunity to work together again, sometime down the road.

To my family, Daddy, Linda, Laura, DiDi, and all your respective spouses and offspring, you have always loved, supported and believed in me, whole-heartedly. Thank you. Even if we don't always share the same ideals, thank you for not letting that

get in the way. Your unwavering love and support have given me a deep-seated conviction that I really can do whatever I want to do. Such a gift—thank you.

To my "chosen family" in San Francisco, thank you for not forgetting about me while I have been absentee in New York. Knowing you guys are behind me gives me strength. My profound thanks especially to Walter Laing, who was my anchor in the chaos for 14 years, and really is my hero. You were there for me when I needed you most, as you are for so many of our friends. You do this not because of what you can get out of it, but because you just do the right thing—despite self-interest. Amazing. I wish you and Hannah all my love and eternal thanks.

Last, but certainly not least, thank you to the two people who have supported me the most, in this monastic endeavor. This is your achievement too. Richard Mortimer Humphrey, thank you for moving to NY to help keep me sane through on the tail end of this crazy marathon. Thank you for the constant supply of hugs and forehead kisses, and for trying to hold back the chaos in our apartment. Also thanks for the coding support, feedback, and fun with robots. I'm looking forward to our next steps together. And finally-- Momma, no one could love, respect and support anyone more whole-heartedly and unconditionally than you have done for me. You are a natural engineer, and have inspired me to be one too. You have taught me not to be afraid of doing things outside the norm. You have always taught me that I can do anything. Thank you for giving me this awesome life.

TABLE OF CONTENTS

LIST OF FIGURES

LIST OF TABLES

CHAPTER 1

INTRODUCTION

As silicon photonics matures and we simultaneously expand our capabilities into new wavelength ranges, we have begun to discover ways to expand what we have learned at telecommunications wavelengths into these new regions. As a consequence, new fields of study are emerging. One area of expansion and cross-pollination is with deep-media imaging, sensing and detection, and the treating of heat from a photonic perspective with the development of devices and techniques familiar to shorter wavelengths, like ring resonators, gratings and photonic crystals. [1,2] This is especially relevant to biological applications like light delivery to deep-tissue. The advantages of multi-photon imaging at the combined scattering and absorption windows, for example, at 1300 and 1700 nm in brain tissue, have been utilized for years. [3,4] But only recently have windows been discovered at longer wavelengths, for example, in thigh tissue at 1.8 μm and in brain tissue as far as 2.2 μm. [5,6] It is generally agreed in the community that these types of discoveries have been slow to develop due primarily to a lack of detectors at longer wavelengths in the mid-infrared.

For wavelengths where the absorption is high, minimally invasive mid-infrared light delivery with integrated detection has the potential to enable many important applications, since the absorption lengths are not limiting to the depth of interrogation. This way the functionality of longer wavelengths is accessible while still reaching deep-media. Mid-infrared endoscopy with large fibers has been shown to be useful for analyzing chemical fingerprints in vivo, especially during surgery. [7–10] But these devices suffer from a lack of integrated detection and from a lack of resolution in part

due to the physical cross-section of the fibers but also functionality due to lack of device integration. [7–10] Also intraoperative thermal imaging, a rapid method to define the boundaries of brain tumors, is restricted by a lack of penetration in the tissue and requires full exposure of a legion. [11] Since heat is mid-infrared light, these thermal methods could be greatly improved with the application of minimally invasive light-delivery and collection techniques for mid-infrared wavelengths. With broad research interests in the brain and increased emphasis on understanding complex biological systems, new fields will continue to develop and expand in these fields, and more generally, in any field where the photonic treatment of mid-infrared light or heat is applicable.

The following is a set of primers to facilitate understanding of the concepts associated with the work in the following chapters. This is intended to be of particular use for people with varied backgrounds, who may not have specific expertise in one or more of these areas. The primers include a mechanical, an optical, and an electrical primer.

Mechanics Primer

Euler Buckling Formula

The dominant failure mode for long narrow beams being inserted into a viscoelastic medium is buckling. The Euler buckling formula describes this mode. [12], [13], [14]

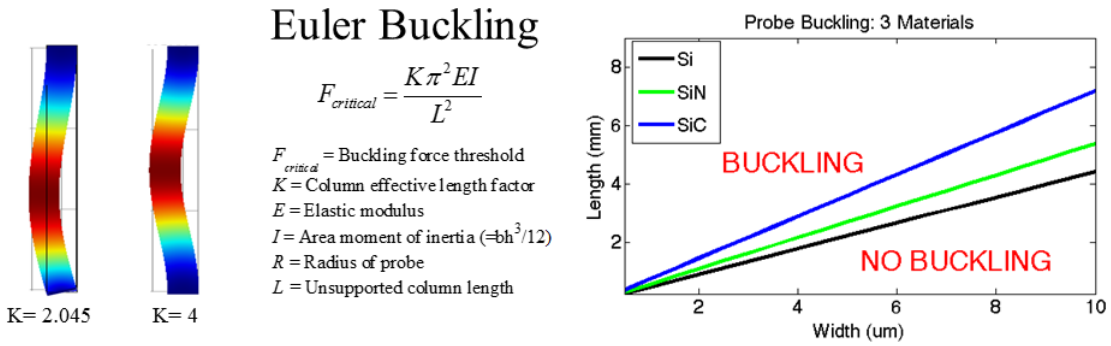

Figure 1.1: The Euler Buckling formula (center) describes when a long, narrow beam will buckle with end loading normal to the tip. On the left are two finite element models demonstrating examples of the K length factors for two sets of boundary conditions, fixed/fixed and fixed/pinned. On the right is a graph of the critical dimensions before a long, narrow beam will buckle assuming the more conservative fixed/pinned boundary conditions.

The longer and/or narrower a beam is, the more likely it is to buckle in response to a force applied at the beam tip. Stiffness is a measure of a beam's cross-section to withstand bending and is both a material and geometric property. (Stiffness = EI) Elastic modulus is purely a material property (E=elastic modulus) and the second moment of inertia is purely a geometric property. I is the second moment of inertia which is equal to the integral of (y^2 dy), where y is the distance from the neutral axis. For a rectangular cross-section I = $bh^3/12$, where b is the width of the cross-section perpendicular to the direction of bending and h is the thickness of the beam in the direction of bending. The width of the beam has a much smaller contribution to stiffness than the thickness.

The boundary conditions, and whether a beam is able to rotate, either at the tip or at the base, play a significant role in whether a beam buckles or not also. If both ends are able to rotate, a beam is most likely to buckle, and if both ends are unable to rotate, a beam is able to resist twice the same force normal to the tip. When one end is fixed and the other is pinned, or able to rotate, the beam's ability to resist buckling is in between the pinned/pinned and fixed/fixed boundary conditions. These properties are present in

the Euler buckling equation with the length factor K. The reason why it is called the length factor is because it scales the actual length to be analogous to the curvature of a simply supported beam in bending which is free to rotate at one end and fixed at the other. For example, a fixed/fixed beam can be broken into 4 sections that each resemble the curvature profile of a beam that is only fixed at one end.

Other Mechanical Considerations

Again the stiffness of the beam is important to how much a beam will deflect in response to a force, either at the tip or from the weight of the beam itself. When fabricating long narrow structures, we want to avoid stiction, which can occur from the beam deflection interfering with the substrate after the release layer is removed between the beam and the substrate. For this reason it is useful to consider how much a beam will deflect from its own weight, in addition to external forces. Although for the work in the following chapters failure in compression or tension is not the primary failure mode, it is important to consider for other device materials and geometries.

Optics Primer

Snell's Law

Snell's Law can be used to determine the relationship between the incident (θ_i) and transmitted (θ_t) angles of a ray traveling from one refractive index (n_1) to another (n_2).

$$n_1 \sin(\theta_i) = n_2 \sin(\theta_t) \tag{1.1}$$

Snell's Law is the reason why when we see something beneath the surface of water, its location is not where it seems to be, as viewed from above the water surface. This is due

to the difference in refractive indices of the air, where we are viewing from, and the water, where the object resides. When a ray is traveling from a high index medium to a low index medium, and the angle of a light ray's incidence on the surface longer transmitted. This is the basis for why optical waveguides work to guide light. Light is coupled into a high index "light pipe" that is cladded with a lower index material. When light rays are incident on this interface at or past the critical angle, all of the light (with the exception of scattering losses and absorption) is reflected back into the waveguide.

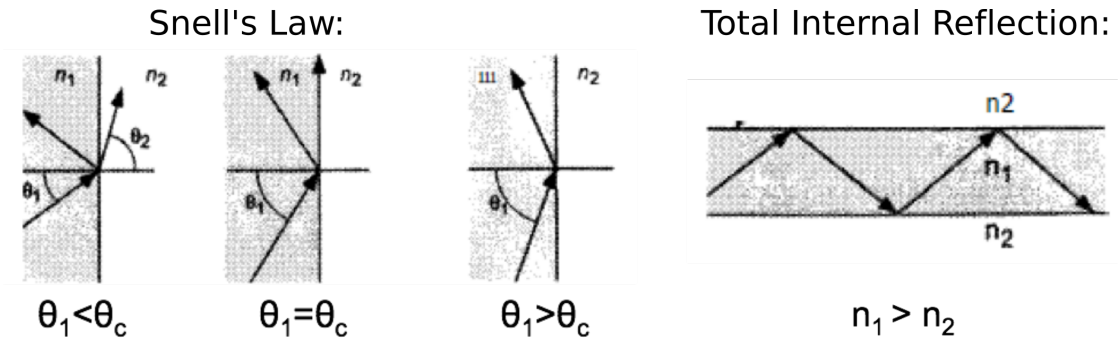

Figure 1.2: Diagrams from **[15]** illustrating Snell's law and total internal reflection past the critical angle θ_c.

Ring Resonator

Ring resonators are a primary building block in silicon photonic devices. By evanescently coupling light from one straight waveguide into a waveguide with a closed ring path, an optical cavity is achieved. When the distance of the round trip around the ring is equal to an integer number of wavelengths of the light coupled into the ring, then these wavelengths experience constructive interference and get brighter in the cavity. In other words, resonance occurs when $2\pi n_{eff}L=m\lambda$, where n_{eff} is the effective index of the waveguide cross-section, L is the round trip length around the ring, m is an integer, and λ is the resonant wavelength.

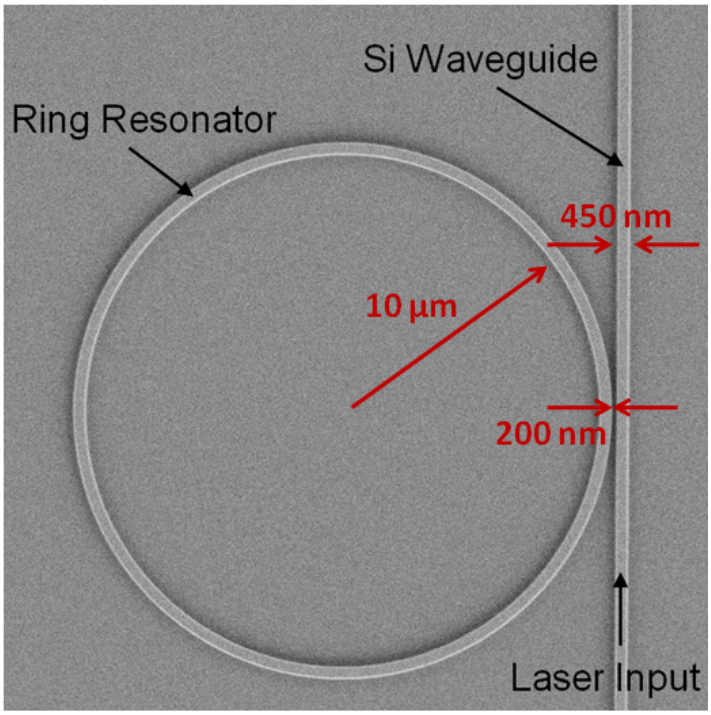

Figure 1.3: SEM image of a typical ring resonator showing the laser input in the bus waveguide, which couples light evanescently across the gap to the resonator (image by Abdurrahman Gumus).

Fresnel Equations

The Fresnel equations arise in part due to Snell's Law, and describe the amplitude and phase of a reflected and transmitted plane wave incident on an interface between two homogenous materials of different refractive index. For TE polarization, or polarization perpendicular to the plane of incident, transmitted and reflected ray vectors: [15]

$$E_{reflected}/E_{incident} = \frac{n_1 \cos\theta_i - n_2 \cos\theta_t}{n_1 \cos\theta_i + n_2 \cos\theta_t} \quad (1.2)$$

Where n_1 and n_2 are the refractive indices the initial media and the transmission media and θ_i and θ_t are the angles of incidence and transmission respectively. For normal incidence, as with coupling light into a waveguide, the equation for Fresnel reflectance

simplifies to $((n_1-n_2)/(n_1+n_2))^2$ where n_1 and n_2 are the refractive indices of the two materials.

Fabry-Perot resonances and losses

Most simply, two opposing mirrors separated by a cavity form a Fabry-Perot interferometer. This cavity's resonant wavelengths occur where the incident light wavelength is equal to an integer multiple of ½ wavelengths in the cavity. The propagation losses in a waveguide can be modeled as the losses in the Fabry-Perot cavity created by the reflections of both the input and output facets. This can be quantitatively measured via transmission and reflection measurements through the waveguide and the data fit according to the following equations: [16], [17], [18], [19], [20], [21], [22]

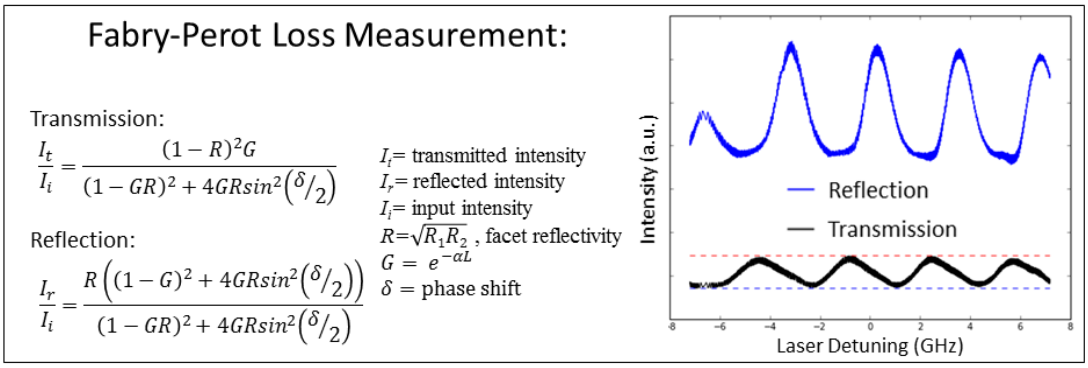

Figure 1.4: The equations for the loss in a Fabry-Perot cavity can be fit to reflection and transmission data to find the propagation loss (α) in the waveguide. This assumes the input and output reflectivities, R_1 and R_2, are equal.

Distributed Bragg Reflector

The constructive and destructive phase characteristics of alternating layers of high and low indices materials can be used to create mirrors. When the thicknesses of the layers are ¼ of the wavelength, the phase constructively interferes in reflection, but still

transmits some light to the next layer, creating an imperfect mirror. A ½ wavelength thickness layer of the low index material can be placed between two of these types of mirrors, forming a cavity that constructively interferes within the ½ wavelength layer and forms a Fabry-Perot interferometer.

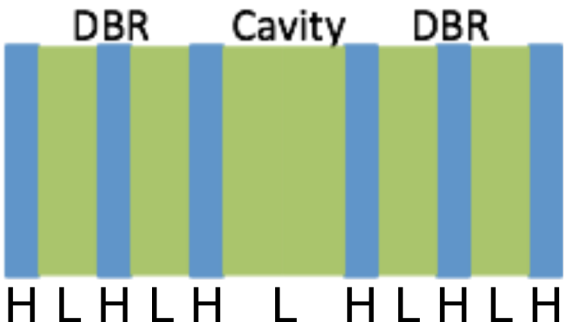

Figure 1.5: Diagram of a DBR cavity showing the orientation of high and low indices materials.

Bragg Grating

Similar to the Distributed Bragg Reflector above, the transmission and reflection of a waveguide can be controlled by alternately varying the width and/or height to alternate between high and low effective indices of the alternating cross-sections, instead of alternating high and low index materials in flat layers. Grating couplers based on this concept can be used to couple light into or out of a waveguide. They are sensitive to both wavelength and to the angle of coupling between the waveguide grating and the exterior media according the following: [23]

$$n_{eff} = n_{top} \sin(\theta_c) + m\frac{\lambda}{\Lambda} \tag{1.3}$$

where n_{eff} is the effective index of the grating, n_{top} is the refractive index of the exterior media, θ_c is the coupling angle with respect to normal to the grating surface, m is the diffraction mode, λ is the wavelength of light incident on the grating, and Λ is the grating period.

Coupling loss

Coupling loss is due primarily to Fresnel reflections (see Fresnel above) and modal overlap. The modal overlap is the area overlap of the mode of an incoming beam with the mode of the mode in the media that the beam in incident on. For example, if coupling light from a lensed fiber of 2.5 μm spot size diameter into a waveguide that has a 10 μm diameter mode in the waveguide, the coupling losses due to modal overlap could be found by integrating over the power overlap of the two modes.

Electrical Primer

Fourier of Pulse Train

The Fourier series for a periodic time-continuous signal is defined by the periodic signal: [24]

$$x(t) = \sum_{k=0}^{\infty} a_k e^{jk(2\pi/T)t} \tag{1.4}$$

where T is the period, t is time, and the Fourier coefficient for the k^{th} harmonic is:

$$a_k = \frac{1}{T}\int_T \mathrm{x(t)}\, e^{-jk(2\pi/T)t}\, dt \tag{1.5}$$

For a periodic square wave pulse train, in terms of sines and cosines this is:

$$x(t) = a_0 + \sum_{k=1}^{\infty} a_k \cos(k(2\pi/T)t) + b_k \sin(k(2\pi/T)t) \tag{1.6}$$

where a_0 is the DC component, a_k and b_k are the Fourier coefficients. This results in the magnitude of each harmonic spectral components equaling:

$$\text{Magnitude}_{\,k} = \sqrt{{a_k}^2 + {b_k}^2} \tag{1.7}$$

When the pulse width of the square pulse is wide the harmonic spectral components follow the sinc function. But when the pulse width is very narrow, as with a femto second pulsed laser source, the magnitude of the harmonic spectral components are flat across a wide bandwidth. This is confirmed by the fact that the Fourier transform of a Dirac function is also a Dirac function.

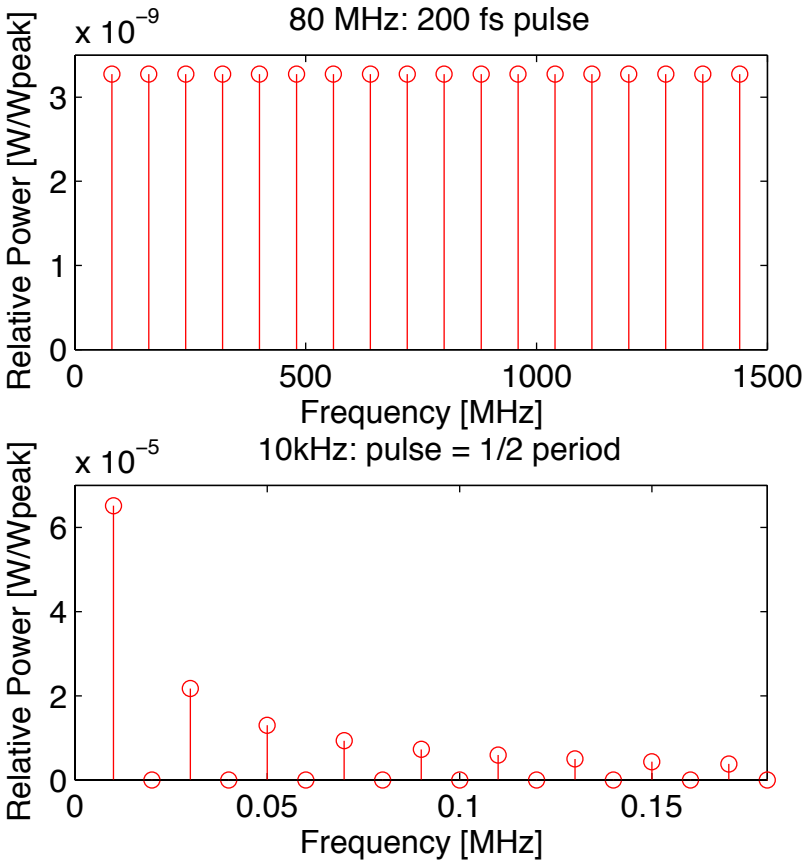

Figure 1.6: Above is the relative magnitude of the spectral components for a 200 femtosecond pulsed laser operating at 80 MHz repetition rate. Below is the relative magnitude of the spectral components for a square pulse that is half the period operating at 10 kHz repetition rate. Both of these graphs are described by the same set of equations describing the Fourier transform of a time-continuous square wave pulse train.

NEP

For an inverse-biased diode the noise equivalent power (NEP) is dominated by the shot noise from background radiation and so follows: [25–27]

$$\text{NEP} = \frac{\sqrt{2eI_{dk}}}{R} \tag{1.8}$$

Loss due to impedance mismatch

In order to avoid or account for measurement losses in the setup due to reflections at higher frequencies, one must take into account losses due to impedance mismatch. The real part of impedance is the resistance R, which can be found from the inverse slope at the operating point of a diode curve. The inductive reactance is $X_L = 2\pi fL$ where L is the inductance. The capacitive reactance is $X_C = {}^{1}/_{2\pi fC}$ where C is the capacitance. The total impedance is $Z = R + j(X_L + X_C)$. By calculating the reflection coefficient $\Gamma=(Z_1 - Z_2)/(Z_1 - Z_2)$ between the two elements with impedances Z_1 and Z_2, the losses in dB due to the mismatch can be found from loss = $-10\log_{10}(1-\Gamma^2)$.

RC limited bandwidth

In a device where the RC (resistance*capacitance) time constant, τ_{RC}, limits the bandwidth, the cutoff frequency is equal to 1/RC where the resistance and/or capacitance can be measured or estimated via calculation. The capacitance of a p/n junction diode is a result of the bias voltage further separating charge with higher biases. Therefore for RC limited devices, capacitance tends to be lower and cutoff frequencies higher for larger bias voltages.

Depletion width: [26]

$$D=\left(\frac{2\varepsilon_r\varepsilon_o V_{bias}(N_A+N_D)}{qN_AN_D}\right)^{0.5} \tag{1.9}$$

Capacitance:

$$C = \varepsilon_r\varepsilon_\circ \text{ Area}/D \tag{1.10}$$

CHAPTER 2

PHOTONIC NEEDLES

Introduction

The use of light for biological imaging and stimulation, has an array of useful applications, but due to combined scattering and absorption effects in tissue, [4], [28] current techniques for optical stimulation and detection in deep tissue require relatively large optical probes and fibers to be implanted, causing significant damage to the tissue. Ground-breaking early light delivery probe schemes, (for example, large chip shank-like designs, [29], [30], [31], [32] reminiscent of traditional electrode on chip platforms, [33], [34] fiber-like devices, [35], [36], [37], [38], [39] or designs with traits of both [40], [41], [42], [43], [44]) are designed to reach deep tissue, but have large cross-sections on the order of 100 μm across or more. Such schemes are destructive to the biological tissue, inducing an immunological response, disrupting the system one would want to measure, and impeding the signal response collected. [45], [46], [47], [48]

The most notable methods attempting to address invasiveness issues while achieving deep tissue light delivery are multiphoton stimulation, [4], [49], [50], [51], [52], [53], [54] and microfabricated multisite light delivery probes. [29], [30], [31], [32] Multiphoton light delivery is minimally invasive, but depths greater than 2 mm are not resolvable without the assistance of more invasive methods. Physical light delivery probes can easily reach multiple data collection sites millimeters deep, but at the expense of very invasive, large cross-sections, on the order of 10's of sites per 10's of cubic millimeters per probe. The large size of these probes makes scaling beyond a few hundred sites problematic. Attempts have been made to miniaturize these

devices, [55], [56], [57], [58], [59], [60] but the tradeoffs remain between accessing deep-tissue, and achieving minimally invasive, high performance light delivery.

We show here a platform for light delivery based on high aspect ratio Photonic Needles – free standing optical waveguides that are long enough to reach deep-tissue, but narrow enough to cause minimal damage. These Photonic Needles have a cross-sectional diameter of only 3 to 10 μm across the entire 3.5 mm length of the probe, displacing orders of magnitude smaller volumes than standard methods. This platform leverages the maturing field of silicon photonics, enabling massively parallel fabrication of photonic structures using CMOS processing.

Methods

In order to overcome the challenge of fabricating these 1000:1 aspect ratio waveguide probes**,** we developed a process based on Mechanical Substrate Removal (MSR). The mechanical removal of the substrate (see Figure 2.1), overcomes the difficulty of chemically removing a thick substrate that is hundreds of microns thick, while maintaining the integrity of the suspended needle that is only a few microns thick. The extremely long etch times needed to remove the entire substrate can penetrate even thick thermal oxide protective release layers and damage the small waveguides beneath, often etching all the way through especially long, small cross-section devices. It is typically difficult to get high yield fabrication of MEMs cantilevers even with much larger cross-sections and shorter lengths. [61], [62], [63], [64] The process we developed involves manually cleaving the substrate away. The process shown in Figure 2.1 starts with an SOI wafer of approximately 3.6 μm of thermal oxide buried beneath approximately 10 μm of crystalline silicon. The Photonic Needle waveguides are patterned using contact

photolithography in widths ranging from 3 to 10 μm wide. The Photonic Needles are aligned perpendicular to the major flat of the <100> wafer, and therefore perpendicular to the crystallographic plane for cleaving the substrate later in the process. A higher elastic modulus could be achieved by similarly aligning along the crystallographic planes in a <111> wafer. After etching the waveguide needles to the buried oxide, a conformal PECVD oxide cladding is deposited to approximately 3.7 μm thick. Then the wafer is diced into single chips using a silicon dicing blade for lower loss facets. Individual chips are then placed into custom machined Teflon holders, which allow for the chip to be vertically submerged in 6:1 BOE. This releases only the Photonic Needle sections to be inserted into biological media in later experiments, and leaves the oxide cladding intact on the other side of the chip for effective optical coupling into the input facets. This release etch does not damage the Photonic Needles, because the etch rate of silicon in BOE is negligible. Next the chip is critical point dried to avoid stiction in contact with the silicon substrate. At this point, the silicon substrate is carefully mechanically cleaved close to the base of the released waveguide probes via Mechanical Substrate Removal (MSR). This is achieved by marking the edge of the substrate close to the oxide base of the released needles with a diamond scribe, and then pushing down on the substrate and away from the released needles, while holding the base of the chip supported on a stack of microscope slides, a few millimeters above the work surface. This leaves a silicon substrate handle approximately 15x5 mm at the base of the Photonic Needles used to insert the entirely released lengths of the needles into the biological tissue. Figure 2.1.b shows the Scanning Electron Micrograph (SEM) of the pristine cleaved silicon face, post-MSR, at the interface between the portion of the chip

where the needles are released and where they are not (left). Note that this pristine surface is in contrast to typical rough etched surfaces resulting from long backside etches. Figure 2.1.c shows the SEMs of both curved (left) and angled (right) Photonic Needle tips, taken from the top of the chip and at a 45 degree angle relative to the chip. Note that the top faces are much smoother than the sides, showing that the sidewall roughness is primarily due to the initial waveguide etch process and not any part of the release process. The dimensions in white are referring to the approximate effective cross-sections, which mediate the critical force for insertion for each tip type, described in further detail in the Results and Discussion section below. The dimensions in red indicate that the patterned radii of all the radiused tips are equal to half the width (d), and that the patterned angle of all the angled tips are at 45 degrees to the length of the needle.

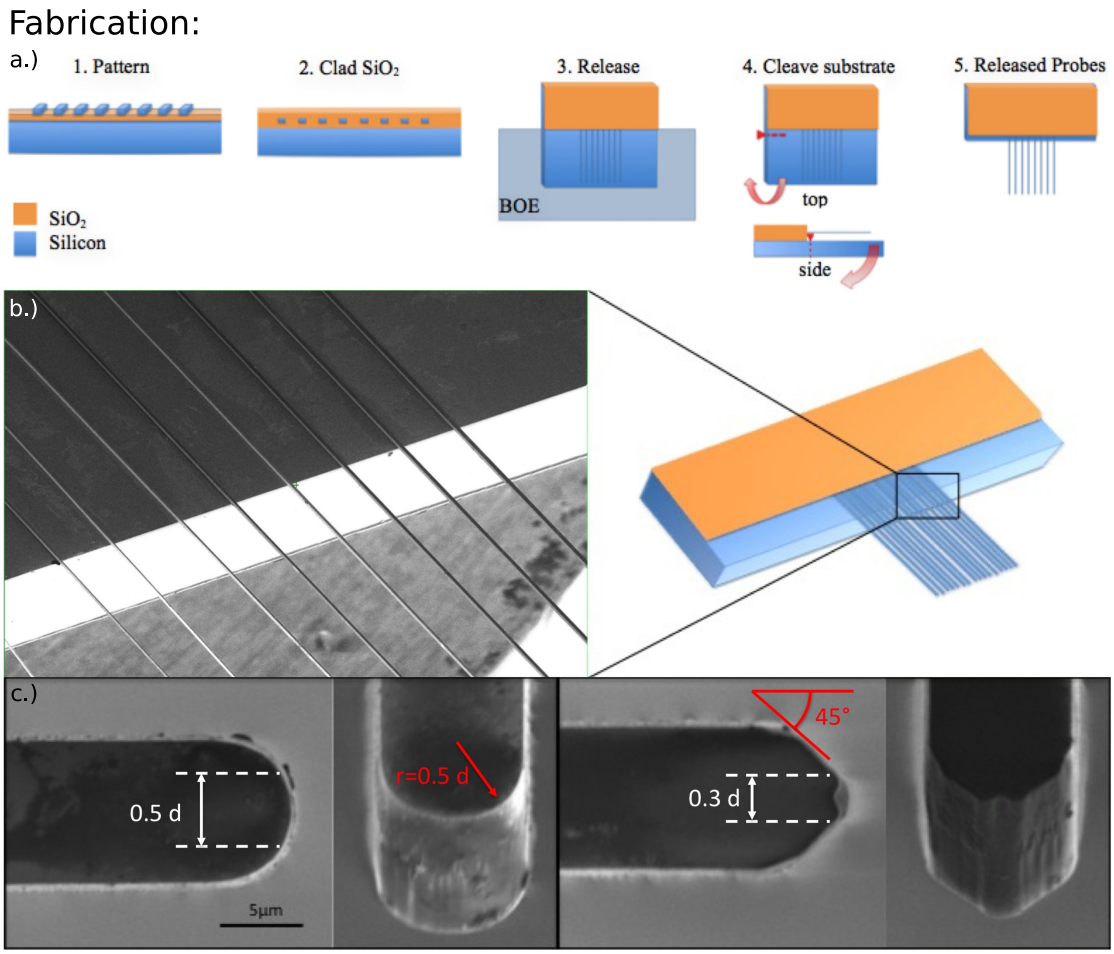

Figure 2.1: Details of the Photonic Needle fabrication using the Mechanical Substrate Removal (MSR) process. a.) Processing steps (left to right): (1) patterning of the Photonic Needle waveguides on the SOI wafer, (2) cladding the waveguides in PECVD oxide, (3) releasing diced chip vertically in BOE, (4) scribing at the base of the released section and mechanically cleaving off the substrate, (5) finally releasing the probes. b.) Scanning Electron Micrograph (SEM) of the Photonic Needles showing the pristine cleaved silicon face, post-MSR, at the interface between the portion of the chip where the needles are released and where they are not released (left). A schematic of the released needles indicating where the SEM was taken is shown on the right. Note that this pristine surface is in contrast to typical rough etched surfaces resulting from long backside etches. c.) SEMs of both curved (left) and angled (right) Photonic Needle tips, taken from the top of the chip and at a 45 degree angle relative to the chip. Note that the top faces are much smoother than the sides, showing that the sidewall roughness is primarily due to the initial waveguide etch process and not any part of the release process. The dimensions in white are referring to the approximate effective cross-sections, which mediate the critical force for insertion for each tip type, described in further detail with the data in Figure 2.4. The dimensions in red indicate that the patterned radii of all the radiused tips are equal to half the width (d), and that the patterned angle of all the angled tips are at 45 degrees to the length of the needle.

Results and Discussion

The optical quality of the Photonic Needles is high, with measured propagation losses of less than 4(+/-)2 dB/cm. This loss is primarily due to the sidewall roughness inherent with contact photolithography, and could be easily improved with deep uv or ebeam lithography. Figure 2.2 shows the estimated propagation losses for 10 μm thick probes with waveguide widths ranging from 5 to 10 μm wide. The propagation loss was extracted by measuring the transmission and reflectivity of the Fabry-Perot cavity created between blunt polished end facets for a 10.2 mm long probe where 3.5 mm of the waveguide length is released and 6.7 mm of the waveguide length is clad (inset shows an example of the transmission and the reflection spectra). [16], [17], [18], [19], [20], [21], [22] The setup consisted of lensed fibers for coupling light in and out of the needles, with a circulator between the source telecom laser at 1550 nm and the needle input facet to measure the reflected intensity data, in addition to the transmitted intensity data collected at the output of the released needle tip. The overall losses were approximately 8 dB on average when coupling with a lensed fiber of 2.5 μm mode field diameter. These losses could easily be improved by minimizing the mode mismatch between the input facets of the Photonic Needle input facets and the fiber input.

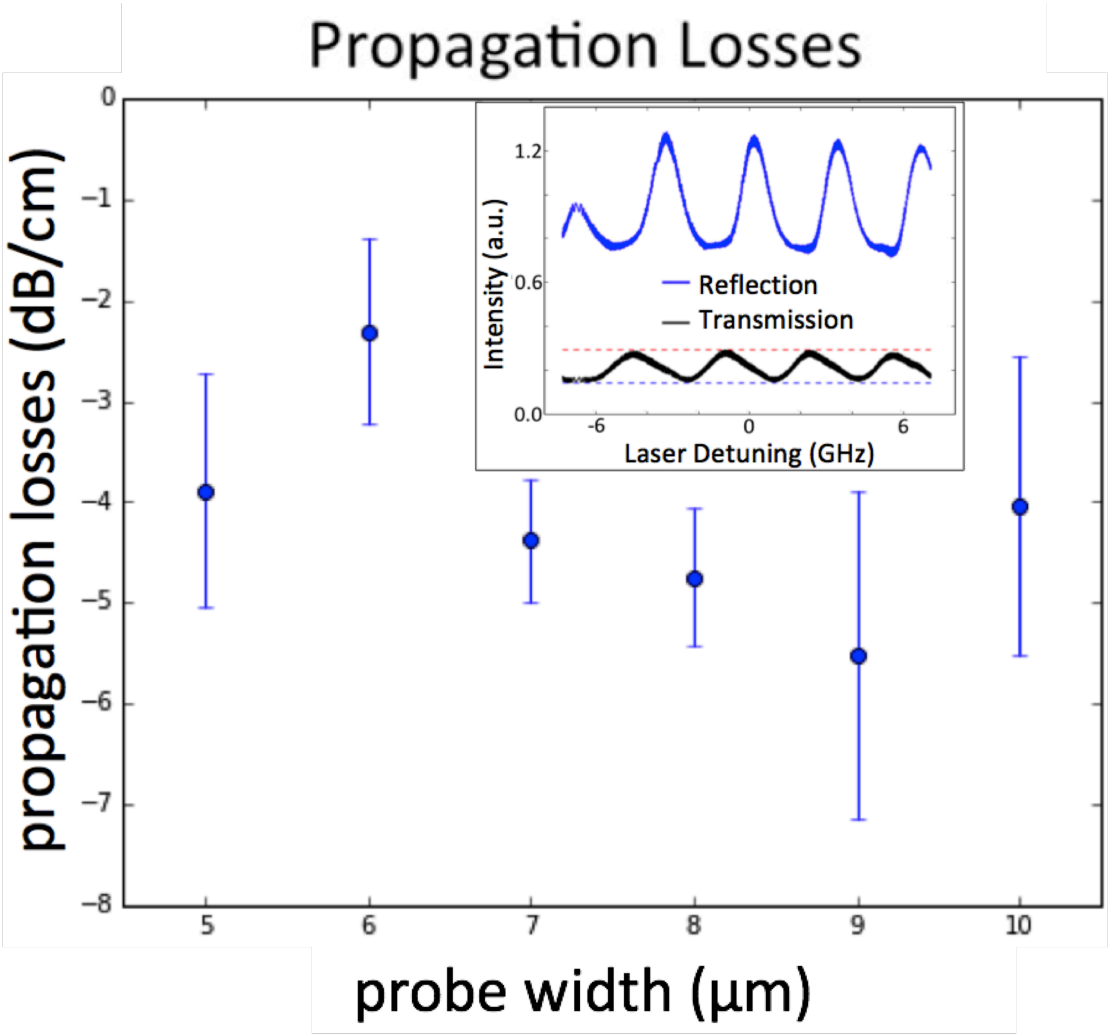

Figure 2.2: Graph shows the estimated propagation losses for 10 μm thick probes with waveguide widths ranging from 5 to 10 μm wide. The propagation loss was extracted by measuring the transmission and reflectivity of the Fabry-Perot cavity [16], [17], [18], [19], [20], [21], [22] created between blunt polished end facets for a 10.2 mm long probe, where 3.5 mm of the waveguide length is released and 6.7 mm of the waveguide length is clad (inset shows an example of the transmission and the reflection spectra).

We determine experimentally the minimal probe cross-section allowed (such that they can be inserted into biological tissue without mechanically failing) to be on the order of 4 μm. In order to answer the question of how small the probe can be before it buckles, we insert the suspended probes into 0.5% and 2% agarose which have been shown to be similar in mechanical properties to mouse cortex without and with dura

intact. [65], [66], [67], [68] The chip holding the array of Photonic Needles was fixed to a 3 axis stage adjacent to a second 3 axis stage with a rectangular cube of agarose. The agarose was supported by a structure of microscope slides on all but the side facing the tips of the Photonic Needles. The needles were inserted by manually actuating the micrometer of one stage towards the other.

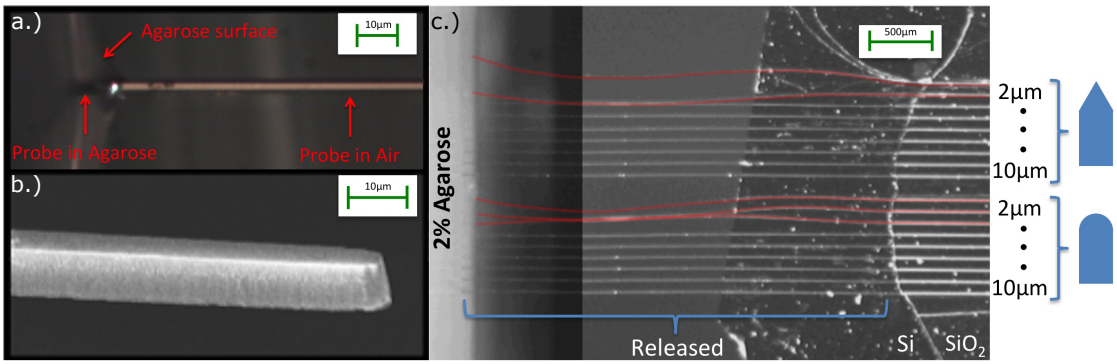

Figure 2.3: a.) Microscope image of a 3.25 mm long suspended probe with 3x10 µm cross-section being inserted into 0.5% agarose by weight, to simulate mouse cortex without dura intact. [65], [67] b.) SEM image of the probe shown in (a.) after release and before insertion. c.) Composite microscope image of released probes with two different tip geometries and widths varying from 2 to 10 µm being inserted into 2% agarose by weight to simulate mouse cortex with dura intact. [65], [66], [67], [68] The Photonic Needles that buckled during insertion are shown in red.

Figure 2.3.a shows a microscope image of a 3x10 µm cross-section probe approximately 3.25 mm long being inserted into 0.5% agarose, with no buckling. Figure 2.3.b is an angled SEM of the same 3x10 µm cross-section probe before insertion. Figure 2.3.c is a composite microscope image demonstrating a full double set of released probes being inserted into 2% agarose. One can see that for the angled tip set, the 2 and 3µm wide needles buckled, but the 4, 5, 6, 7, 8, 9, and 10 µm wide needles did not. For the curved tip set below, the 2, 3, and 4µm wide needles buckled, but the 5, 6, 7, 8, 9, and 10 µm wide needles did not. Buckling needles are colorized in red. Figure 2.4 shows the theoretical maximum Photonic Needle lengths (for a range of widths) above

which buckling occurs for the inserted waveguides with both angled (green) and rounded (blue) tips and our experimental data. We expect that the tip geometry effects the critical cross sectional dimension, because the angled tip will effectively have a smaller area pushing into the surface of the flexing viscoelastic medium than a rounded tip. The theoretical curves are obtained using Euler's buckling equation [12], [13], [14]

$$F_{critical} = \frac{K\pi^2 EI}{L^2} \tag{2.1}$$

where K is the column effective length factor determined by the boundary conditions, E is the elastic modulus, I is the area moment of inertia (=base*height^3/12), and L is the unsupported column length. $F_{critical}$ is the estimated force needed for insertion in the brain tissue of a mouse cortex with dura intact from previous studies [67], [68] (scaled for cross-section) to be on the order of 74 μN for a 5x10 μm blunt tipped needle. The boundary conditions in our experiments are somewhere in between fixed/fixed (K=4) and fixed/pinned (K=2.045) end conditions, since dimpling of the viscoelastic surface will provide some imperfectly rigid resistance to rotation at the tip. Therefore, both boundary conditions are shown bounding the theoretical values expected here. To the right of Figure 2.4 are finite element (FEM) rendered beams buckling for fixed/pinned and fixed/fixed boundary conditions (not to scale). The experimental data in Figure 2.4 shows the dimensions extracted from our experiments where buckling occurred (red cross) and no buckling occurred (circle). The mixed point represents dimensions where the rounded tip needle buckled and the pointed tip needle did not buckle. From the data, one can see that the widths for which buckling occurred were less than 4(+/-)1 μm, corresponding to what is predicted by the theory.

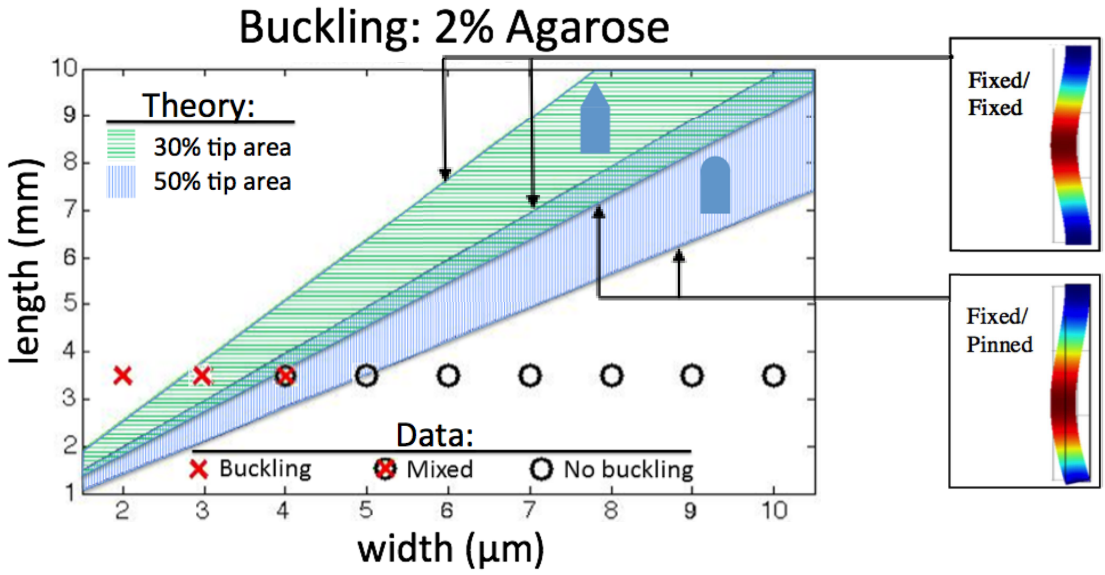

Figure 2.4: Maximum Photonic Needle lengths above which buckling occurs (for a range of widths). The range of waveguide lengths derived from theory assumes the boundary conditions are somewhere between fixed/fixed and fixed/pinned for the inserted waveguides with both pointed and rounded tips (, respectively). Dimensions were extracted from our experiments for buckling and no buckling conditions (, respectively). The mixed point ( ) represents dimensions where the rounded tip needle ( ) buckled and the pointed tip needle ( ) did not buckle. Right are finite element (FEM) rendered beams buckling for fixed/pinned and fixed/fixed boundary conditions (not to scale). Arrows point to the curves describing each boundary condition assumption enclosing the theoretical range of critical dimensions for each tip geometry.

We expect that even longer Photonic Needles could be inserted in biological medium without buckling if composed of materials such as silicon nitride and silicon carbide, whose higher elastic moduli (E) contribute to larger stiffnesses. The graph in Figure 2.5 shows the critical length as a function of cross sectional size considering silicon (E=220 GPa), silicon nitride (E=250 GPa), and silicon carbide (E=450 GPa). One can see that a 3.5 mm long probe composed of silicon is expected to buckle at a width of approximately 6 µm while the same probe, composed of SiC with the same geometry would not buckle. We assume here a conservative blunt tip geometry, as well as a

pinned/fixed boundary condition (K=2.045) instead of the fixed/fixed boundary condition (K=4).

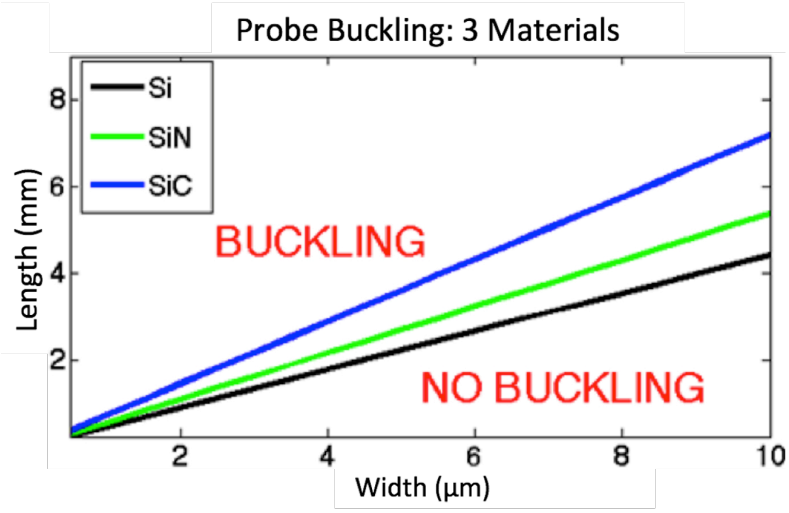

Figure 2.5: Critical length as a function of cross sectional size, considering silicon (E=220 GPa), silicon nitride (E=250 GPa), and silicon carbide (E=450 GPa). One can see that a 3.5 mm long probe composed of silicon is expected to buckle at a width of approximately 6 μm while the same probe, composed of SiC with the same geometry would not buckle. We assume here a conservative blunt tip geometry, as well as a pinned/fixed boundary condition (K=2.045) instead of the fixed/fixed boundary condition (K=4).

Conclusion

We demonstrate the concurrent mechanical and optical robustness of up to 3.5 mm long Photonic Needles with cross-sectional dimensions down to 5 μm wide by 10 μm thick. These Photonic Needles could be used, for example, as light delivery probes for multi-photon imaging, excitation and collection, or as a substrate for much smaller waveguides designed for low loss at visible wavelengths. Also the fabrication concepts demonstrated in this work are easily transferrable to numerous other materials and etch chemistries. This platform leverages the mature fields of both micro electro mechanical systems and silicon photonics. In fact, similar needle-like platforms have recently been

shown for electrical probing, [69], [70], [71] demonstrating how these Photonic Needles could enable a new scalable platform with 100's or even 1,000's of light delivery sites and/or other electrical or mechanical elements, by displacing only a negligible volume of tissue.

Additional Data:

Table 2.1: List of propagation loss values and standard deviations for each needle width from 5 to 10 μm. The overall average is 4(+/-)1 dB/cm.

Needle Width [μm]	Propagation Loss [%]	Standard Deviation [%]	Propagation Loss [dB/cm]	Standard Deviation [dB/cm]
5	0,60	0,11	-3,9	-1,2
6	0,42	0,13	-2,3	-0,9
7	0,64	0,05	-4,4	-0,6
8	0,67	0,05	-4,7	-0,7
9	0,73	0,10	-5,5	-1,6
10	0,61	0,13	-4,0	-1,5
Averages:	0,61	0,10	-4,1	-1,1

Transgenic Mouse Experiments

In vivo 3-photon imaging experiments were attempted using a pulsed laser source at 1700 nm after the insertion of an aggregate of needles. An aggregate was inserted due their being wetted with saline prior to insertion, allowing for the surface tension of water to pull them together. Figure 2.6 shows how the launching of light into a single needle via a large mode area fiber into the input facet of the needle helped maintain the soliton for delivery to the imaging site. Figure 2.7 shows the fluorescence data collected at various depths of needle insertion. The overall depth of insertion was approximately 3 mm.

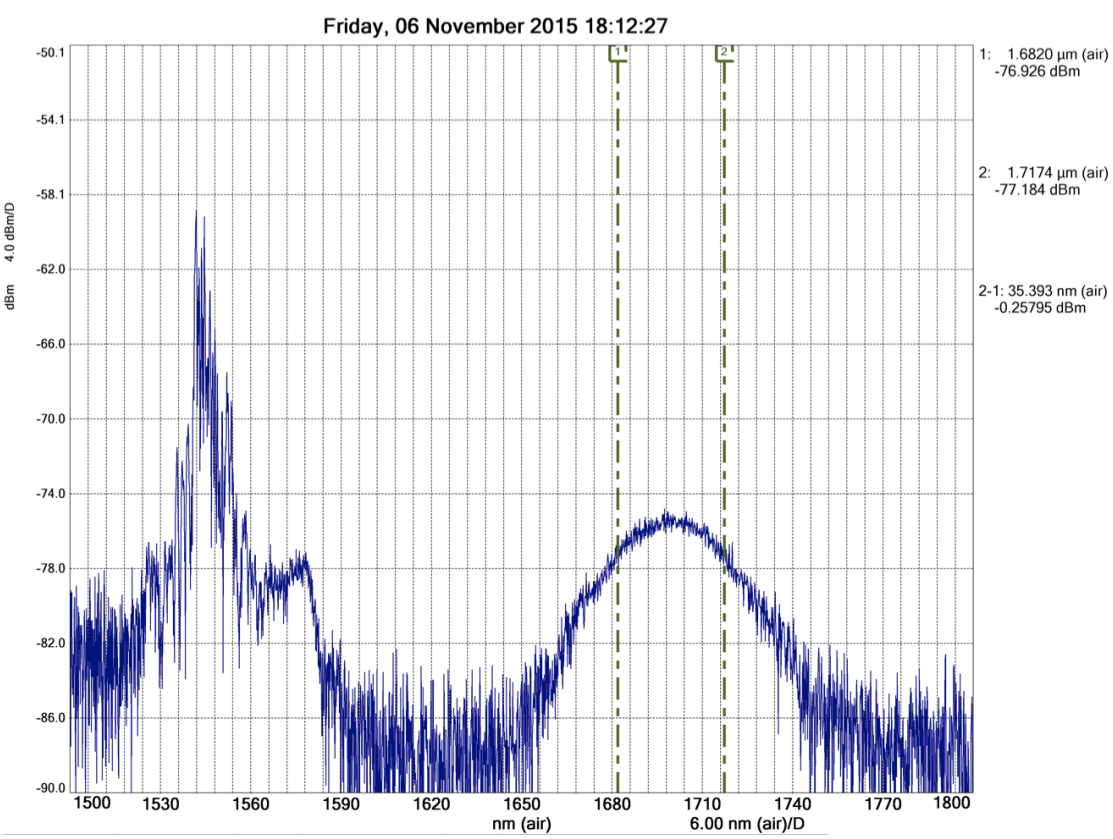

Figure 2.6: Spectral output from the Photonic Needle tip shows the soliton coming out of the needle at ~1700nm has 6mW in the soliton with 20 mW total and a 35 nm pulse width. The soliton directly out from LMA fiber (the input to the Photonic Needle) is at ~1710nm has 18 mW in the soliton with 60 mW total and a 44 nm pulse width.

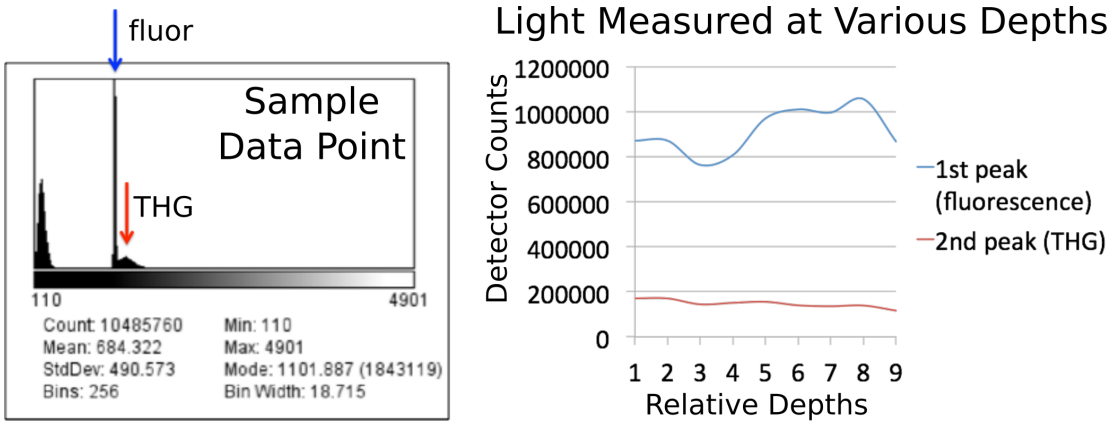

Figure 2.7: 3-photon fluorescence data taken at various depths shows a strong signal at the fluorescence (fluor) wavelength expected inside the brain. Also there is a third harmonic generation (THG) peak that is most likely the contribution from input fiber light overshooting the Photonic Needle and exciting the surface of the brain directly. The x-axis of the sample point histogram (left) represents pixel intensity, which is proportional to either fluorescent or THG signal strength. The fluorescent and THG channels are measured using band-pass filters in front of photomultiplier tubes for each respective measurement. The total depth at point 9 (right) is approximately 3 mm.

CHAPTER 3

INTEGRATED MID-INFRARED DETECTOR

Introduction

The growing need for applications like thermal energy harvesting, telecommunications and spectroscopy has fueled the recent advancements in mid-infrared (mid-IR) silicon photonics; however, efficient and broadband silicon waveguide-integrated detectors have not yet been demonstrated past 2.5 μm wavelength. Previous studies have successfully demonstrated efficient mid-IR detectors based on III/V, II/VI, and IV/VI compounds, like PbTe [72], MCT [73], PbSe [74], HgTe [75], InAs [76] , GeSn and GeSi [77–79], or based on novel material structures like graphene [80–82], quantum dots [74–76,83] and surface modifications in silicon [84]. What all of these detectors have in common is that they rely on materials that are difficult to integrate with silicon photonic platforms. These limitations have fueled the need for a silicon based mid-IR detector that can be monolithically integrated with the existing silicon photonic platform.

The fundamental challenge with developing a silicon detector for the mid-IR is that longer wavelengths have lower photon energies ($h\nu \sim 0.18$ to 0.62 eV) as compared to the available bandgap in silicon ($E_g \sim 1.1$ eV). Recent demonstrations have shown that one way to overcome this challenge is to use dopants like zinc [25], boron [85], silicon divacancy (Si+) [86,87], and argon [88] to create mid-bandgap states in silicon. But the responsivity of these devices diminishes with longer wavelengths, and none have been demonstrated beyond 2.5 μm. This excludes many essential wavelengths for many

applications, including on-chip spectroscopy and most of the "molecular fingerprint" region. [89] There are minimally 100's of molecular species with particularly strong spectroscopic absorption lines in just the 3 to 4 μm range alone. [90] Development of a silicon based integrated detector with high responsivity from 2 to 7 μm would have a strong impact towards realization of a spectroscopic platform that could be implemented in ubiquitous environments.

In this work, we show the first waveguide-integrated silicon photodiode demonstrated in the wavelength range from 3.36 μm to 3.74 μm. [Fig.1] In order to achieve a broadband mid-IR photodetector in silicon, we introduce an extrinsic sulfur dopant into what would otherwise be an intrinsic silicon photodiode (PIN becomes PEN). [91–93] The sulfur dopant introduces mid-bandgap energy states, primarily at 0.318 eV and 0.18 eV from the conduction band. [94,95] [Fig. 1a] Figure 1a is an energy band diagram showing how the smaller energy gap allows mid-IR photons, with energies much lower than the silicon bandgap, be excited into the conduction band. The spectral response of the sulfur dopant is expected to peak near 5.5 μm, and extend from 2 to 7 μm at greater than 30% of the peak response. [93] Our photodiode is integrated in a silicon waveguide such that there is high optical mode overlap with the sulfur dopant. [Fig. 1b] The Silvaco simulation in Figure 1b shows an approximation of the net dopant concentration of the waveguide cross-section, and the Comsol simulation in Figure 1c shows the optical mode at 3.8 μm for the same 3 by 3 μm ridge waveguide with a 1.7 μm thick slab. The gray lines in Fig. 1b correspond to the 1/e and $1/e^2$ power values for the optical mode in Fig.1c, and show that the area interacting with the optical mode is relatively evenly sulfur-doped in the range of $10^{16}/cm^3$ to $10^{18}/cm^3$ concentration. The large waveguide

cross-section enables high optical confinement, lower scattering loss along the length of the device and less absorption interaction with the metallic contacts, enabling a higher efficiency response.

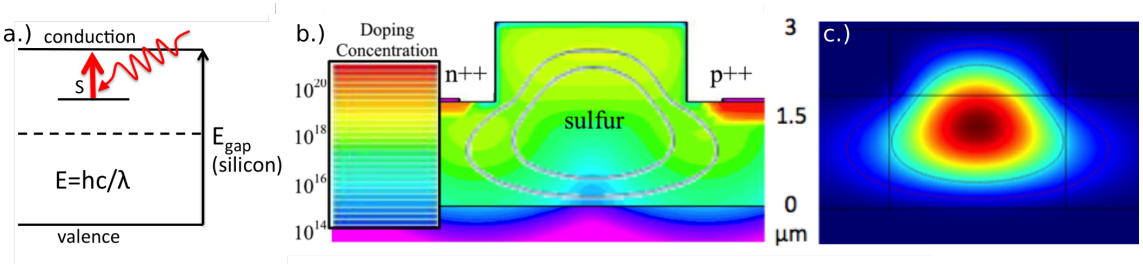

Figure 3.1: (a.) Simplified energy diagram for the detector shows the mid-bandgap state created when silicon is doped with sulfur. The energy transition is smaller therefore corresponds to longer wavelengths. (b.) Silvaco simulation results of net dopant concentration in the waveguide after activation with gray lines corresponding to the 1/e and $1/e^2$ power values for the optical mode in Fig.2b shows that the area interacting with the mode is relatively evenly sulfur-doped in the range of $10^{16}/cm^3$ to $10^{18}/cm^3$. (c.) Comsol simulation of the optical mode in waveguide for wavelength of 3.8 μm shows the over lap of power in the mode with the doped region in Fig.2a.

Fabrication

We fabricate the sulfur-doped mid-IR photodiode using standard silicon photonics fabrication techniques. Fig.2 is a microscope photograph showing a top view of the mid-infrared photodectector with sulfur-doped waveguide section horizontally across the center between phosphorus and boron doped n++ and p++ regions above and below waveguide. The red arrow indicates where the light is coupled into the waveguide and propagates in the direction of the waveguide-integrated detector. We use a silicon-on-insulator (SOI) wafer with 3 μm thick, high resistivity Float-Zone silicon device layer with a 3 μm buried oxide layer. As shown in Fig. 3, we pattern waveguides using contact photolithography and dry etch the waveguides using inductively coupled plasma reactive

ion etching (ICP-RIE). We then pattern resist exposing the location of the detector (the 200 μm waveguide section including 500nm on each side of the section). This area is shallowly implanted with a total dose of 3e14 cm^{-2} sulfur ions at 190 keV, and annealed at 1050C (480 min.) to heal the crystal and diffuse the dopants deeper throughout the waveguide. Annealing at high temperatures preferentially produces the mid-bandgap states at 0.318 eV and 0.18 eV which we are targeting with this design. [94] A 3 μm plasma-enhanced chemical vapor deposition (PECVD) silicon dioxide cladding layer is then deposited, followed by a via etch through the oxide to define the metal contact and p/n doping regions. We then pattern the p/n doping of the ohmic contacts, 200 μm long by 10 μm wide, along each side of the waveguide. The p++ and n++ ion implantation here is at 6e15 cm^{-2} dose, and at 5 and 10 keV for the p++ and n++ respectively. A reflow anneal at 500C (15 min.) and 900C (30 min.) is followed by a rapid thermal anneal at 1050C (0.4 min.) to heal the crystal and activate the dopant species. The target result is sulfur dopants in the desired region of the waveguide with concentration on the order of 10^{17} cm^{-3}, and p++ and n++ contact regions on the order of 10^{20} cm^{-3} at the contact surface, as approximated in our Silvaco simulation [Fig.1b]. Finally, we deposit metal contacts consisting of a molybdenum silicide/titanium/aluminum stack to complete the ohmic contacts for the diode. Note that it is important for this deposition to happen after the annealing steps to avoid melting the metals while reaching adequate activation temperatures for the dopants. The resistance and capacitance of these devices were measured to be on the order of 100 kΩ and 1 nF respectively.

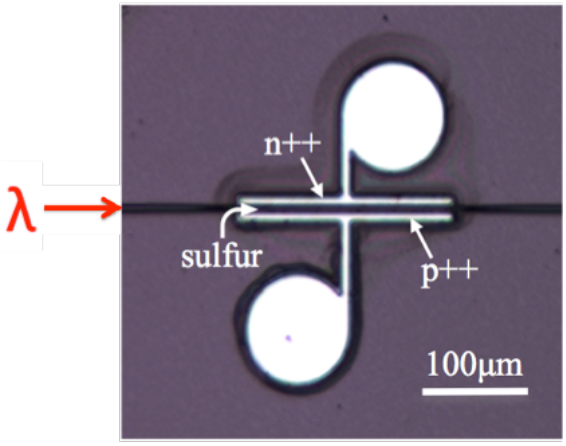

Figure 3.2: Microscope photograph shows a top view of the mid infrared photodetector with sulfur-doped waveguide section horizontally across the center between phosphorus and boron doped n++ and p++ regions above and below waveguide. The red arrow indicates where the light is coupled into the waveguide and propagates in the direction of the waveguide-integrated detector.

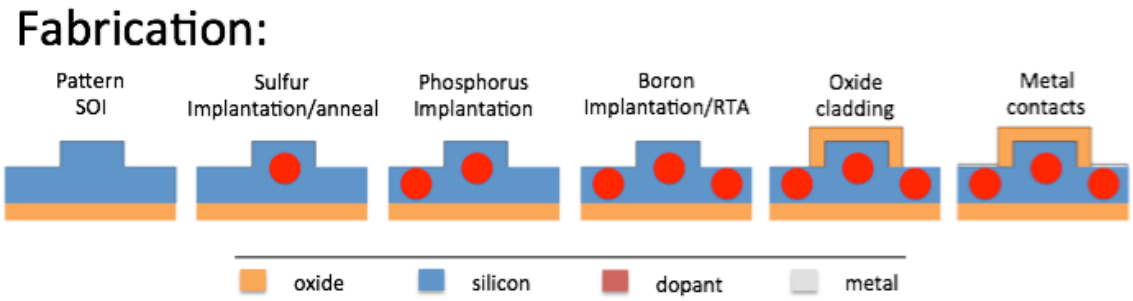

Figure 3.3: Fabrication of these waveguide integrated detectors starts with an SOI wafer, with patterned ridge waveguides. Next the sulfur is implanted and the wafer is annealed to distribute the dopant across the waveguide cross-section. Then the n++ and p++ contact regions of the diode are implanted with phosphorus and boron respectively, and then rapid thermally annealed to activate the dopants. Lastly the oxide cladding is deposited, vias etched for the metal contacts, and the metals deposited to complete the ohmic contacts.

Results/Discussion

We measure a responsivity of 28 +/-2 mA/W with a 30 V reverse bias at 3.74 μm and obtain a spectral response from 3.25 to 3.74 μm with increasing responsivity at longer wavelengths. This responsivity is on the same order of magnitude as longer length waveguide detectors measured from 2.2 to 2.4 μm. [25] To measure the responsivity of our detector, we use a mid-IR laser source (Argos Model 2400 CW optical parametric oscillator) that is tunable from 3.2 to 3.8 μm, and couple light into the chip using an aspheric lens. We measure in input coupling loss of 24dB into the chip to determine the power incident on the detector. The responsivity and dark current are shown vs. bias voltage in Fig. 4a and Fig 4a inset. Figure 4 shows the noise equivalent power (NEP) calculated for various biases and across the wavelengths from 3.3 to 3.74 μm. At 3.7 μm wavelength the NEP was measured to be 4.3e-10, 1.9e-10, and 1.4e-10 W/√Hz at 10, 20, and 30 V reverse biases respectively. [Fig.4b] These figures are of the same order of magnitude of other waveguide detectors at 2.2 to 2.4 μm, but are more constant across the wavelengths measured. [25] The NEP improves at larger reverse bias, despite the increasing dark current, because the simultaneous increase in responsivity has larger contribution of the to the overall NEP. The NEP as a function of wavelength for reverse bias voltages greater than zero is:

$$\mathrm{NEP}(\lambda, \mathrm{V}) = \frac{\sqrt{2e * Idk(\lambda, \mathrm{V})}}{R(\lambda, \mathrm{V})}$$

where Idk and R are dark current and responsivity respectively as a function of wavelength and reverse bias voltage. [25–27]

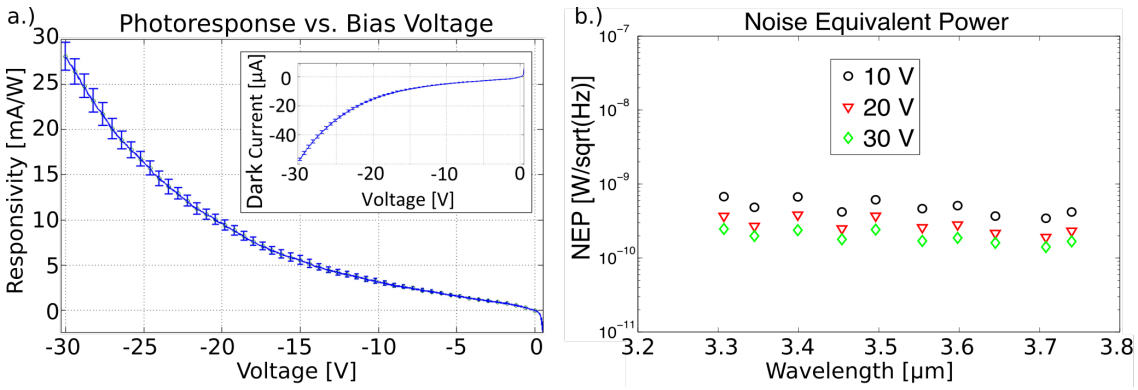

Figure 3.4: a.) The responsivity graph shows a peak responsivity of 28+/-2 mA/W with a -30V bias at 3.74 μm. The inset graph shows the dark current measurement at various bias voltages for the same device. b.) The noise equivalent power is shown to decrease with increasing reverse bias voltage from 3.3 to 3.74 μm, with a value of 1.4e-10 W/√Hz at 30 V reverse bias at 3.7 μm.

In order to rule out nonlinear carrier generation from the silicon itself, we measure the responsivity vs. optical power and find a linear response as seen in Fig. 5a. This linearity also confirms that this device is not operating in the avalanche regime, which is reasonable considering the operating voltage is far from the measured catastrophic breakdown voltage at 66 V reverse bias. In Figure 5b, we vary the laser wavelength and measure responsivity vs. wavelength. The upward trend in responsivity for longer wavelengths is consistent with the dopant responsivity curve seen in previous literature. [93] The dotted line in Figure 5b is meant as a guide to the eye and not to suggest the significance of a linear fit.

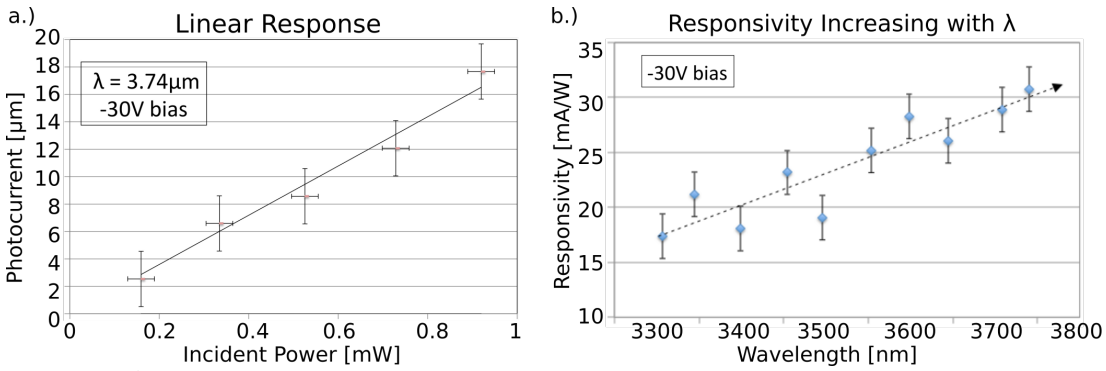

Figure 3.5: a.) The responsivity with respect to wavelength graph shows the increasing response at longer wavelengths as expected from previous literature. [93] The dotted line is not meant to indicate a linear fit, but just serves as a guide to the eye. b.) The photocurrent with respect to incident power onto the detector shows the linear trend, excluding a contribution from non-linear processes like the free carrier generation in intrinsic silicon at shorter wavelengths.

Conclusion

Further studies on alternative device geometry, as well as on the doping recipe with respect to annealing/activation temperatures, times, and ion implantation concentrations could likely yield designs optimized for specific performance parameters. These devices could be optimized for higher collection efficiency, and therefore higher responsivity, by placing the contact regions closer to the center of the waveguide. Figure 1c shows the high optical mode confinement with these devices and how the contacts could likely be moved closer to the center of the mode by 1 μm or more before any significant absorption from the metals would occur. Also the capacitance could be minimized with a thinner slab and therefore a smaller cross-section depletion region, decreasing the RC of future devices. It is likely that responsivity and bandwidth could both be increased with higher sulfur doping concentrations closer to the insulator metal transition at around 10^{20} cm^{-3}, and multiple groups have recently demonstrated how this might be achieved via processes like hyperdoping and laser annealing. [96–99]

We have demonstrated the first waveguide-integrated silicon detector at the wavelength range 3.36 μm to 3.74 μm with just a single CMOS compatible doping step added to the fabrication process. We have measured responsivity up to ~30 mA/W at 30 V reverse bias voltage, and NEP as low as 3e-10 W/√Hz at 3.74 μm. Further optimization of the doping recipe and physical detector geometry will open up increased performance applications for high speed and low noise detection in silicon. We see this technology as an important first step towards enabling, for example, on-chip spectroscopy, mid-infrared photonics research, and thermal sensing, by providing a low cost and simply integrated detection solution in a wavelength range where there are currently few options available.

CHAPTER 4

OTHER INTEGRATABLE DEVICE ELEMENTS

Ring Resonator Gas Sensor in the Mid-Infrared

We fabricated and measured resonances of ring resonators designed to sense gas via light absorption in the mid-infrared. Figure 4.1 shows a photo of these mid-infrared ring resonators with a window in the oxide cladding over the resonators, exposing the rings so that gas in the environment can interact with the resonant mode. Figure 4.2 shows the measured resonances of the air clad resonators at around 2.3 μm with multiple resonances across a broadband laser source input to the resonators (above) and a zoom into a few of the resonances (below). The rings were designed for approximately 2.5 and 3.3 μm where there are there are a number of gasses with strong absorption resonances including Methane. The simulation in Figure 4.3 shows more than 3 dBm change in transmission at 3.3 μm in a methane rich environment.

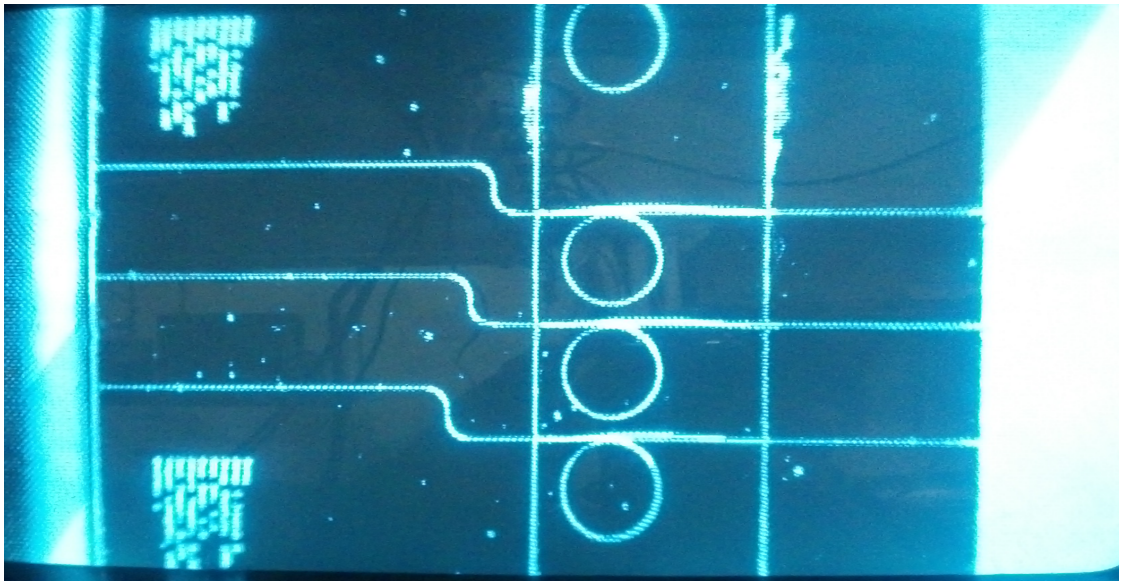

Figure 4.1: Photo of mid-infrared ring resonators showing the window in the oxide cladding over the resonators, exposing the rings so that gas in the environment can interact with the resonant mode.

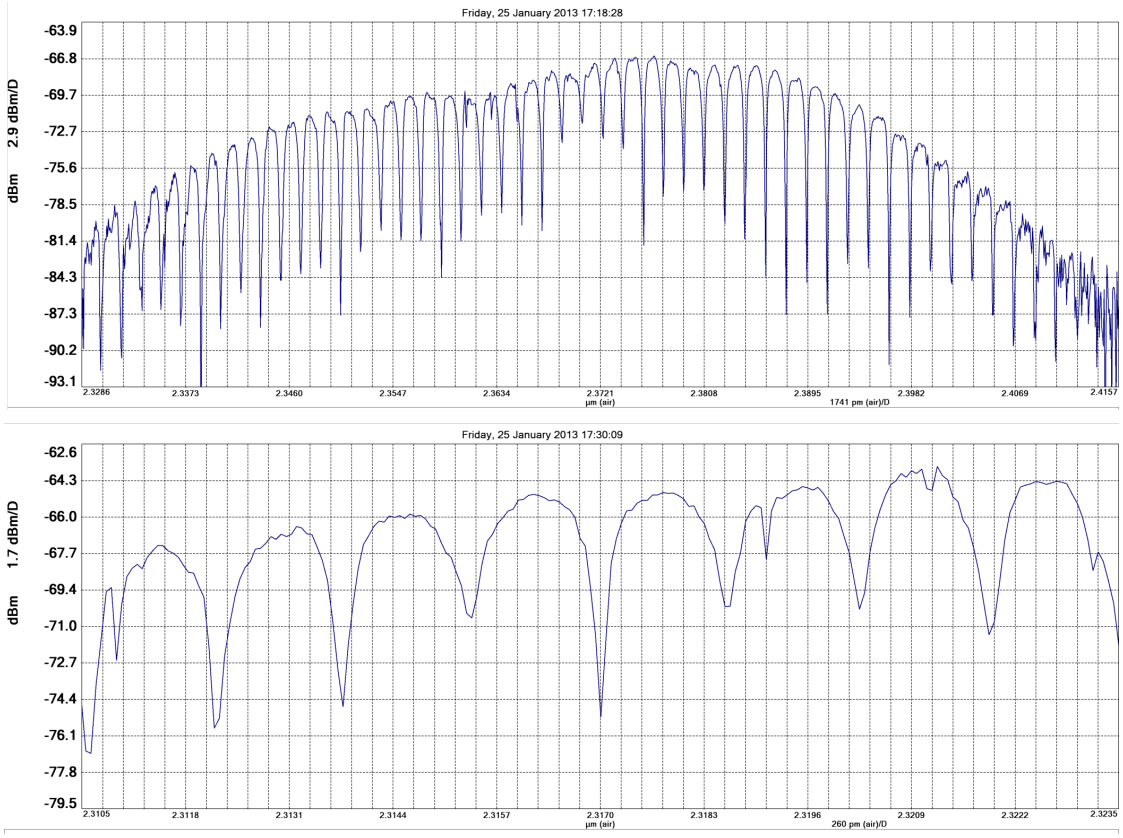

Figure 4.2: Measured resonances of the air clad resonators at around 2.3 µm show multiple resonances across a broadband laser source input to the resonators (above) and zoom into a few of the resonances (below).

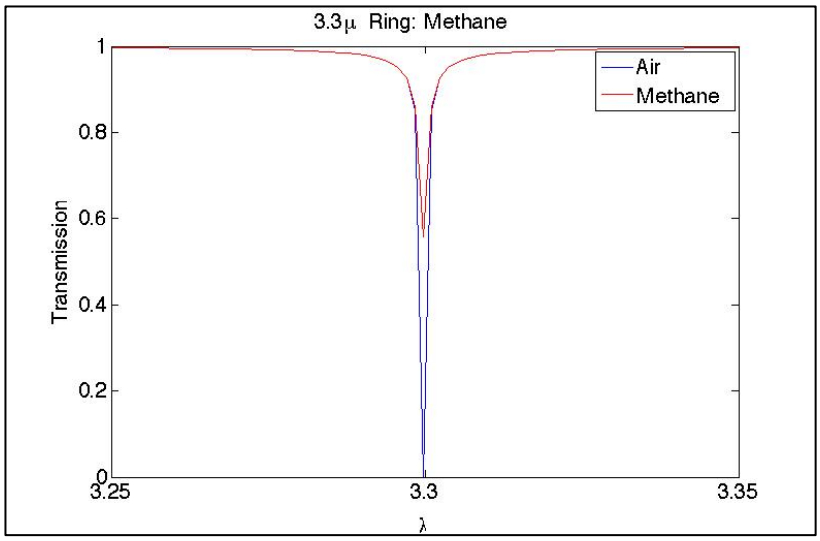

Figure 4.3: Simulation results show more than a 3dB change in transmission at 3.3 μm in a methane rich environment.

Optical Parametric Oscillator in Silicon at 3.8 μm

We fabricated, from a standard 3 μm device layer SOI wafer and inline with our integrated mid-infrared detector from Chapter 3, a dispersion engineered ring resonator with ohmic contacts to remove free carriers as with [72]. [

Figure 4.4] Figure 4.5 is a graph of dispersion versus wavelength for a 3 x 3 μm ridge waveguide with various slab heights. The datapoint on the graph indicates anomalous dispersion at approximately 50 ps/(nm km) for a slab 1.7 μm, equal to slab height of the actual fabricated devices.

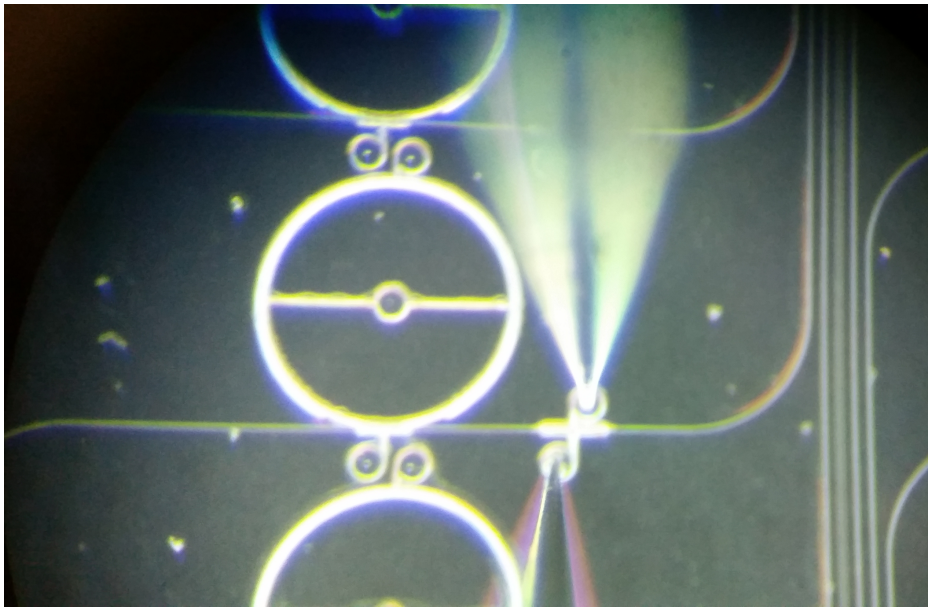

Figure 4.4: Microscope image of an OPO in line with the mid-infrared detector from Chapter 3. Contact regions surrounding the ring are for removing free carriers similar to [100].

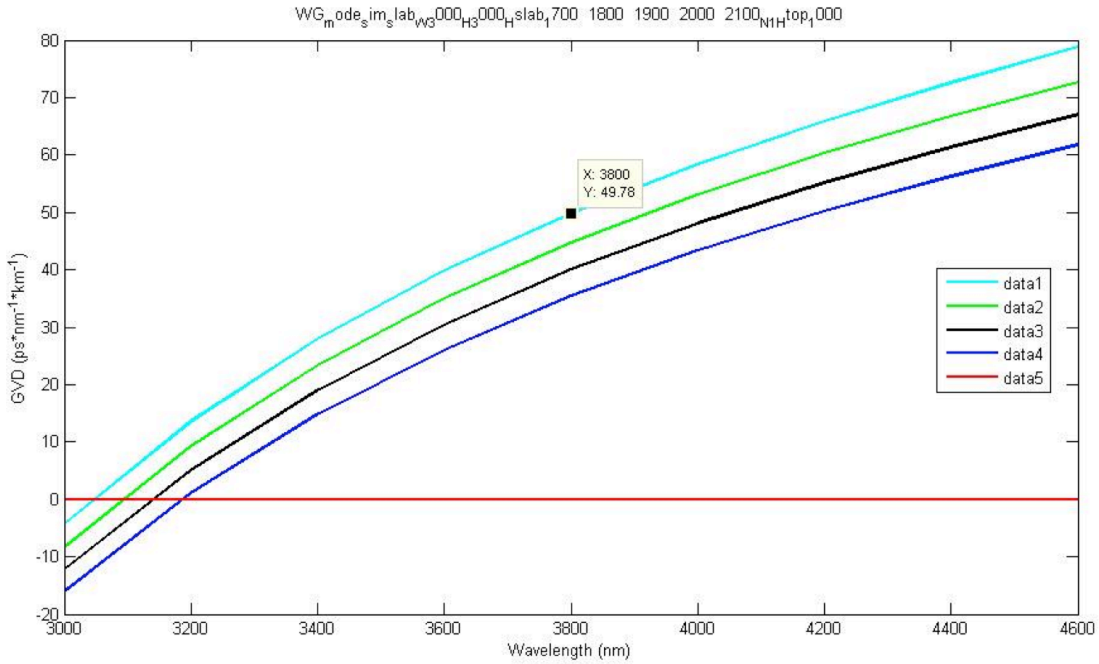

Figure 4.5: Dispersion graph for a 3 x 3 μm ridge waveguide with varied slab heights shows anomalous dispersion approximately equal to 50 ps/(nm km) for a slab height of 1700 nm.

Weak Electric Field Sensor

We fabricated and began initial testing of a set of MOEMS devices to sense electric fields on the order of 1V/m in various environments, including water, electrolyte, and air. We also attempted an even lower spring constant by patterning 200 nm spring member widths to achieve smaller than 1V/m resolution. The design is based on a DBR resonant cavity (see Optics Primer, Chapter 1). Two DBRs are separated by a gap with a thin metal layer on top, which is penetrable to incident light used to probe the resonance of the cavity from the top. The top Bragg mirror of the resonator with the thin gold layer is suspended by serpentine springs on 4 sides. The dimensions of these springs are designed to have a spring constant which allows the deflection of the top mirror 1 μm when electrostatic force of 1 V/m is applied to the gold film. The spring model is based on the models from [101] where a and b (as seen in Figure 4.7 to Figure 4.10) are the lengths of the members parallel and perpendicular, respectively, to the straight sides of the gold film. Resonance measurements of a few AIR devices showing resonance at 1.42 μm is seen in Figure 4.11.

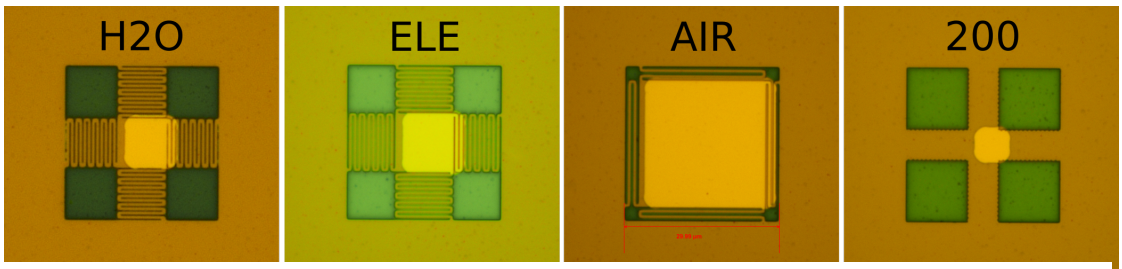

Figure 4.6: Microscope photographs of MOEMS electrostatic actuators to measure electric fields on the order of 1 V/m in various environments, including water, electrolyte and air.

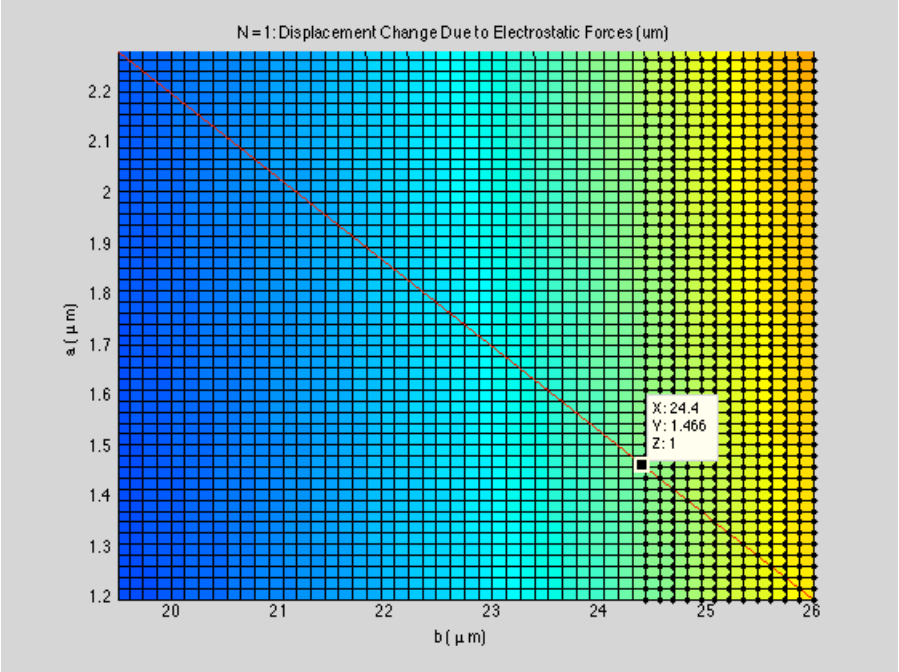

Figure 4.7: 3D graph of the spring model based on the models from [101] in air (AIR) where a and b are the lengths of the members parallel and perpendicular, respectively, to the straight sides of the gold film. The data point shows the dimensions of a and b which result in a 1 µm mirror displacement. The widths of these members is 400 nm.

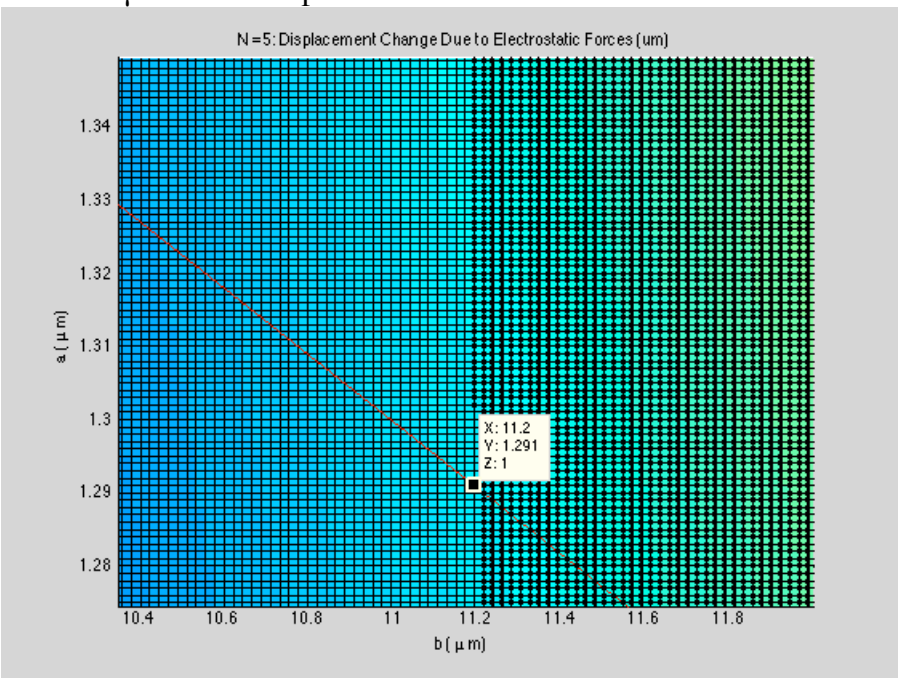

Figure 4.8: 3D graph of the spring model based on the models from [101] in electrolyte (ELE) where a and b are the lengths of the members parallel and perpendicular, respectively, to the straight sides of the gold film. The data point shows the dimensions

of a and b which result in a 1 μm mirror displacement. The widths of these members is 400 nm.

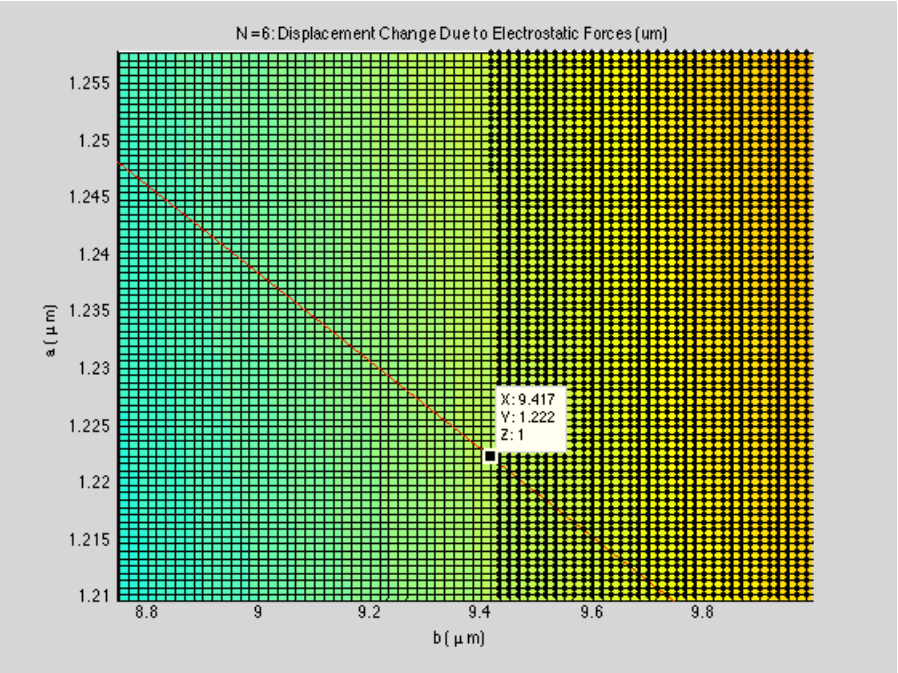

Figure 4.9: 3D graph of the spring model based on the models from [101] in water (H2O) where a and b are the lengths of the members parallel and perpendicular, respectively, to the straight sides of the gold film. The data point shows the dimensions of a and b which result in a 1 μm mirror displacement. The widths of these members is 400 nm.

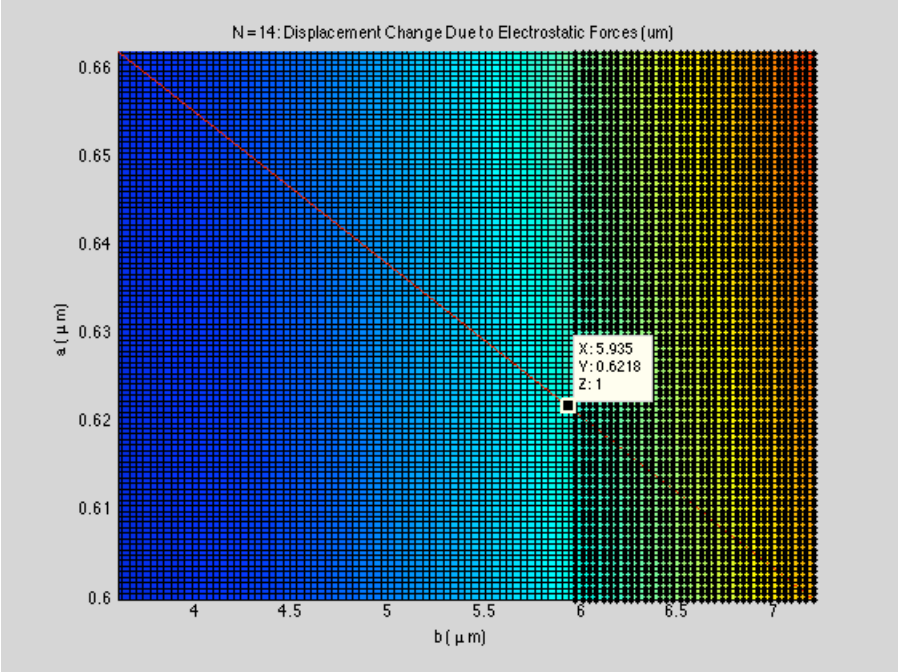

Figure 4.10: 3D graph of the spring model based on the models from [101] in where a and b are the lengths of the members parallel and perpendicular, respectively, to the straight sides of the gold film. The data point shows the dimensions of a and b which result in a 1 μm mirror displacement. The widths of these members is 200 nm.

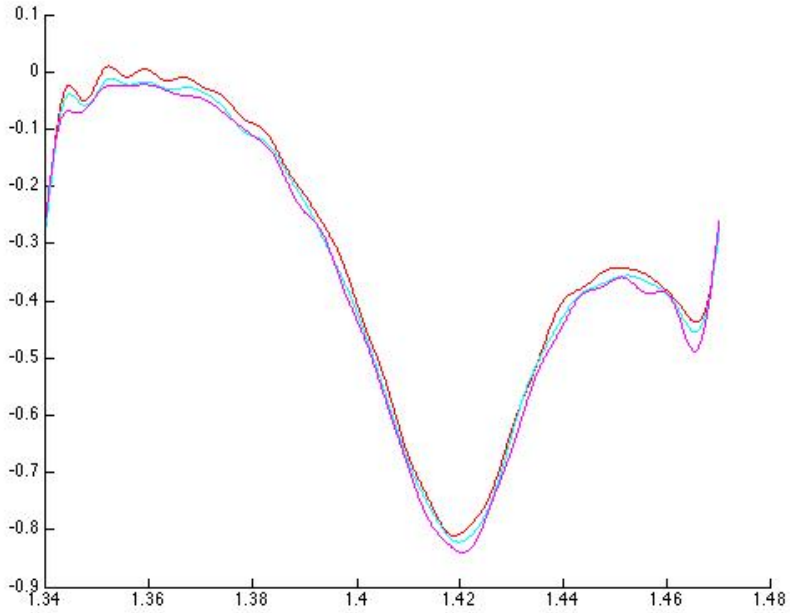

Figure 4.11: Resonance measurements of a few AIR devices showing resonance at 1.42 um.

Gratings

Bragg gratings [see ***Optics Primer***] are, like ring resonators, building block elements of many silicon photonic devices. Integrating gratings, either on waveguides of a different material on the surface of our silicon Photonic Needles [pg.13], or as part of the existing silicon waveguide needles, is a simple and well-understood topic. Figure 4.12 describes functionality which could be implemented as part of integrating gratings with the Photonic Needles, including how different wavelengths could couple into or out of each grating according to its angular orientation to the activated neuron. Figure 4.13 shows simulations of a 1.8 mm long waveguide grating that is continuously chirped so that different wavelengths are scattered at different points along the length.

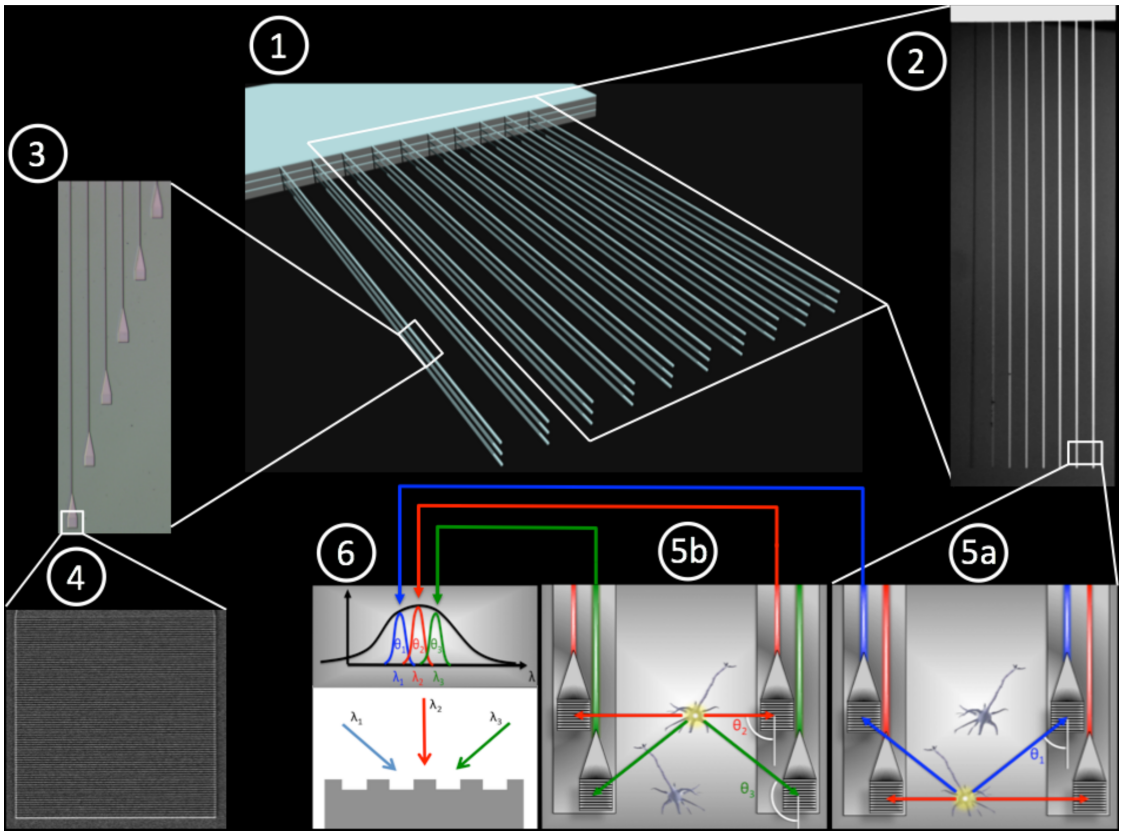

Figure 4.12: 1. Blender rendering describes 10 x 3 array of 10 µm x 10 µm x 3.5 mm long photonic probes. 2. Microscope photo of 8 silicon photonic needles 3 µm to 10 µm

wide, released into air with no substrate attached below. 3. SEM image of a set of 6 nitride waveguides terminating into gratings, which are sensitive to angle, and wavelength. 4. Close up SEM image of a single nitride grating. 5. Diagram expands a section of 2 probes with 2 gratings on each. (grating fabrication and photographs by Aseema Mohanty) 5a. Case 1: Neuron 1 is firing and its position is triangulated with angles gleaned from the wavelengths coupling into each grating, at the angle indicative of that wavelength. 5b. Case 2: Neuron 2 is firing and, similarly, the position is triangulated via the wavelengths collected, but with different angles, wavelengths, and position. 6. Graph describing the broad spectral bandwidth available from the excitation of a neuron, and the more narrow wavelengths associated with different angles incident on the grating.
Different wavelengths will couple into each grating according to its angular orientation to the activated neuron.

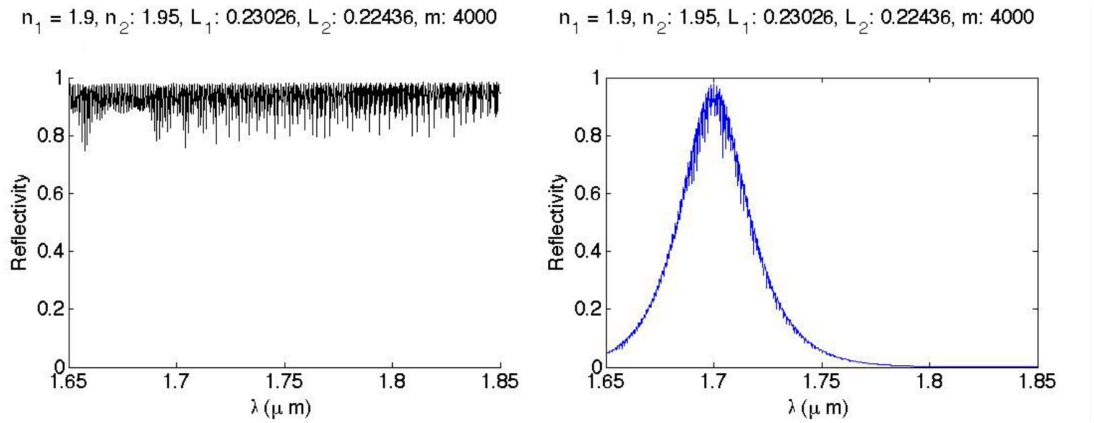

Figure 4.13: Matlab simulations of a continuously chirped grating show the overall reflectivity (left), and in response to a 70 femtosecond pulsewidth laser source (narrow pulse width in time means broadband width spectrally). n_1 is the effective index of the larger width, n_2 is the effective index of the smaller width, L_1 is the length of the larger width, L_2 is the length of the smaller width, m is the number of grating periods. The full length of the grating is m*(L1+L2) = 1.8185 mm.

CHAPTER 5

FUTURE DIRECTIONS

Measuring Detector Speed in the Mid-Infrared

Although the detectors in Chapter 3 are RC limited, future detectors could easily be fabricated with much smaller capacitance and could conceivably have much faster response. This has been observed with other mid-bandgap dopants in silicon like the silicon divacancies (Si+) from [87]. Therefore concerns about carriers getting stuck in mid-bandgap trap states and restricting bandwidth is at least not the case for all mid-bandgap states. Also sulfur doped silicon has the possibility of being more thermally stable past a few 100 degrees and therefore applicable in many more environments. [102] We show here how to easily measure the bandwidth of future devices with a pulsed laser source in the mid-infrared and a spectrum analyzer.

Despite the non-existence of a modulator for the mid-infrared, we measure the RC limited bandwidth for the devices in Chapter 3 at 3.25 μm by measuring the high speed spectral components of an 80 MHz pulsed laser source with a spectrum analyzer, combined with a measured DC response to define the flat part of the Bode plot. [Figure 5.1.a] The measurement setup consists of a 200 fs pulsed optical parametric oscillator with an 80 MHz repetition rate, freespace coupled into our waveguide-integrated detector. High-speed RF probes landed on the p++ and n++ contacts connect to the Picosecond PulseLabs PSPL5547 bias tee where a Keithley 2400 source meter is used to provide the bias voltage via the DC inductive arm and the Agilent E4407B spectrum analyzer is used to measure the oscillating part of the signal via the RF capacitive arm.

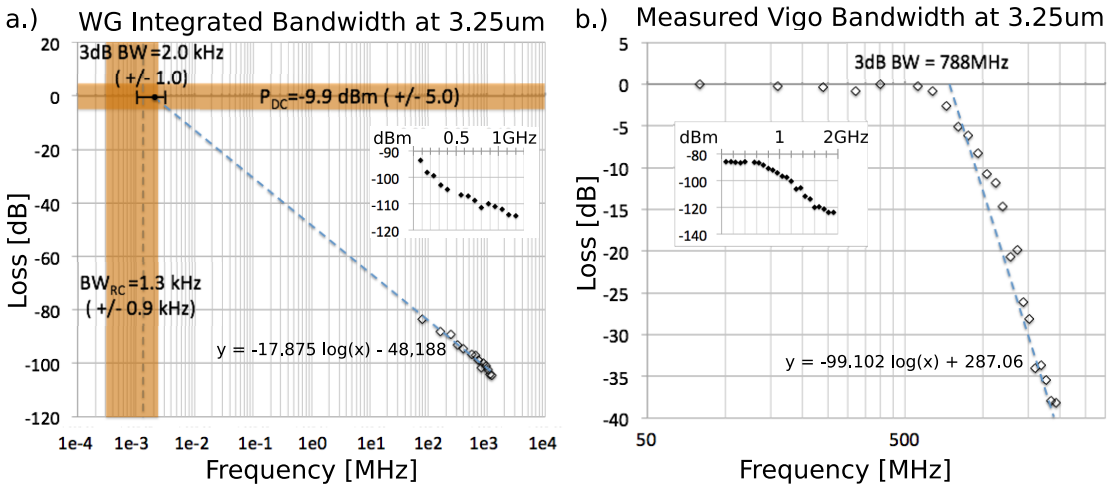

Figure 5.1: a.) The Bode plot for our waveguide-integrated detector (with error range) shows a 2 (+/-1) kHz bandwidth, which agrees with the RC limited estimate from measurement of resistance and capacitance directly. The rolloff slope is measured via the spectral components of an 80 MHz 200fs pulsed laser source incident on the detector, as measured with a spectrum analyzer. The flat DC portion of the Bode plot is defined by the power from the photogenerated current response. The horizontal error bar at the intersection of the rolloff slope and the 0dB line refers to the error in the frequency measurement from the spectrum analyzer (2% of the measurement span =200Hz). Inset is a linear graph of the data at from the spectrum analyzer measurement. b.) The Bode plot for a commercial detector demonstrates the simplified method to measure the bandwidth for detectors with a rolloff past the input repetition rate of the pulsed laser source. Inset is a linear graph of the data at from the spectrum analyzer measurement.

The 80 MHz 200 fs pulsed source can be modeled as a pulse train which has a flat frequency response over a wide bandwidth. [24] Because the 200 fs pulse is short, the Fourier transform of the pulse into frequency domain is broad. The pulse train can be approximated as a Dirac function where the Fourier transform of a Dirac function in time is a Dirac function frequency. This can be demonstrated by taking the Fourier transform of a wider square wave pulse width, whose spectral components follow the sinc function, and slowly decreasing the pulse width until the spectral components flatten over a broad frequency range. This flat response makes the definition of the

rolloff slope a simple measurement on a spectrum analyzer. An equivalent DC response measurement, corresponding to the power at the spectrum analyzer provides the flat portion of the Bode plot as shown with our integrated silicon detector in Figure 5.1.a. The intersection of the DC flat portion at 0dB, and the extended rolloff slope (dotted line) give us an approximate 2 (+/-1) kHz bandwidth for this RC limited detector. This measurement is verified with RC estimates via direct measurements of resistance and capacitance. The small signal resistance was measured to be approximately 70(+/-21.7) kΩ from $dV/dI_{photocurrent}$ at the operation point of 30 V on the IV response curve for this particular device. The capacitance due to the voltage dependent depletion width was measured at 1.8(+/-0.23) nF at 30 V inverse bias.

For a detector with a bandwidth surpassing the repetition rate of the laser source, the entire Bode plot can be gleaned from the spectrum analyzer data alone. For example, in Figure 5.1.b we demonstrate this technique by measuring the bandwidth of a Vigo PVI-4TE mid-infrared detector (amplified, cooled MCT in freespace package). The 3dB bandwidth of the commercial detector is 788 MHz at 3.25 μm wavelength.

Photonic Needles in Other Materials/Other Wavelengths

There are many materials with higher elastic modulus, as well as lower absorption for certain wavelengths, than the silicon used for the Photonic Needles in the work from Chapter 2. Because of this fact, smaller cross-section and/or longer needles could be fabricated with the same stiffness as these silicon needles as seen if Figure 5.2. Also this platform can be optimized in part by choosing materials with low absorption in a particular wavelength range. The following is one example of how this could be

realized in silicon nitride and with visible wavelengths, but the same concepts apply to other materials and other wavelength ranges.

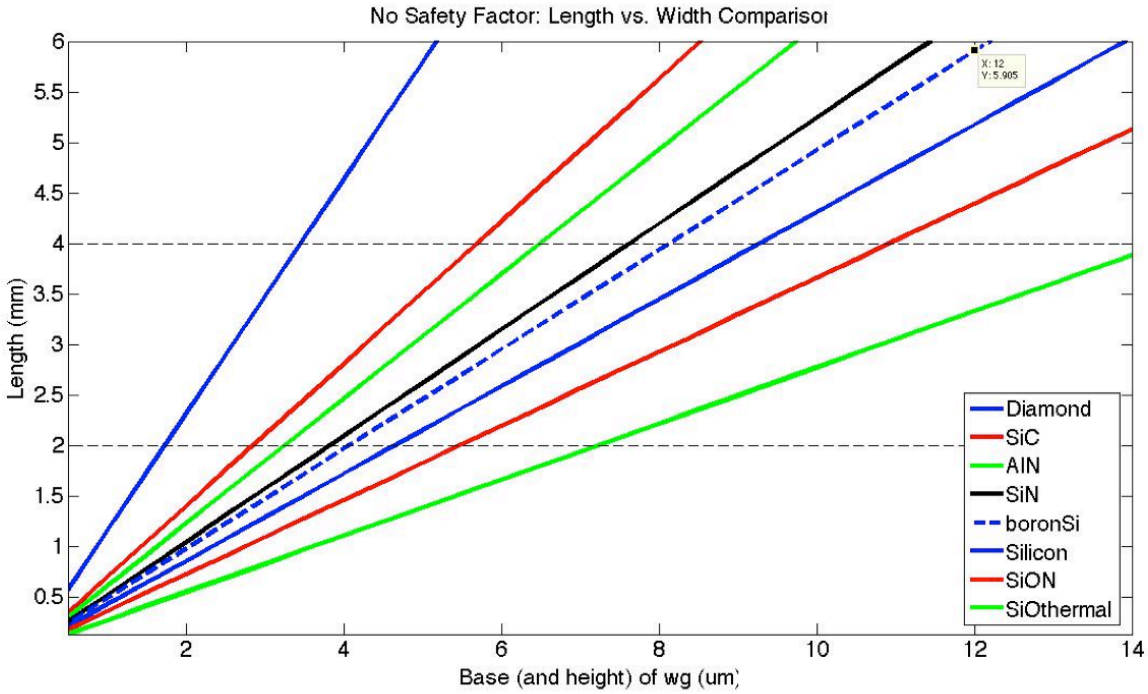

Figure 5.2: Graph of length versus cross-section dimension for needles of various materials shows that particular materials would be more or less robust to failure by buckling according to Euler bucking. Assumptions for this graph are the more conservative fixed/pinned boundary conditions and a blunt tipped needle.

Table 5.1: Values for elastic moduli and refractive index for various optical materials suggest more or less desirable materials at infrared and visible wavelengths.

λ		SiO thermal	SiON	Si	Si3N4	TiO2	AlN	SiC	Diamond
	Elastic Modulus								
	E(GPa)=	70	122	169	250	283	345	450	1220
					310			450	
								700	
	Refractive Index								
1675nm	n =	1.44	1.47	3.47	1.98	2.45	2.12	2.59	*2.38*
530nm		1.46	1.49	4.2	2.03	2.52	2.16	2.67	2.42
	Stiffness/ index								
1675nm	E^.25/n=	2.01	2.26	1.04	2.01	1.67	2.03	1.78	2.48
530nm		1.98	2.23	0.86	1.96	1.63	2.00	1.73	2.44

We show the silicon Photonic Needles platform extended to silicon nitride for two recipes, standard PECVD nitride and a low-stress nitride recipe from [103]. The stress was measured in each film recipe prior to needle fabrication by measuring the curvature of the wafers on a profilometer. The standard nitride was approximately 400 MPa and the low-stress nitride was 80-100 MPa. The standard recipe for PECVD nitride is known for having higher residual stress in the material due to the thermal mismatch between silicon and silicon nitride. Due to this residual stress, the needles in this material curved significantly upward after release, making measurement and testing applications difficult. The low-stress nitride curved much less after release and therefore some initial testing could be performed with the needles in this material. The losses for longer wavelengths were significantly lower than for shorter wavelengths. Figure 5.3 shows a broad-spectrum 488nm light source transmitted through a low-stress nitride Needle. The 488nm source looks mostly greenish but it includes wavelengths from blue to red. The tip looks mostly red because the nitride absorbs much less of the red light than the blue light. This is likely due to the low-stress nitride being more silicon rich than standard silicon nitride.

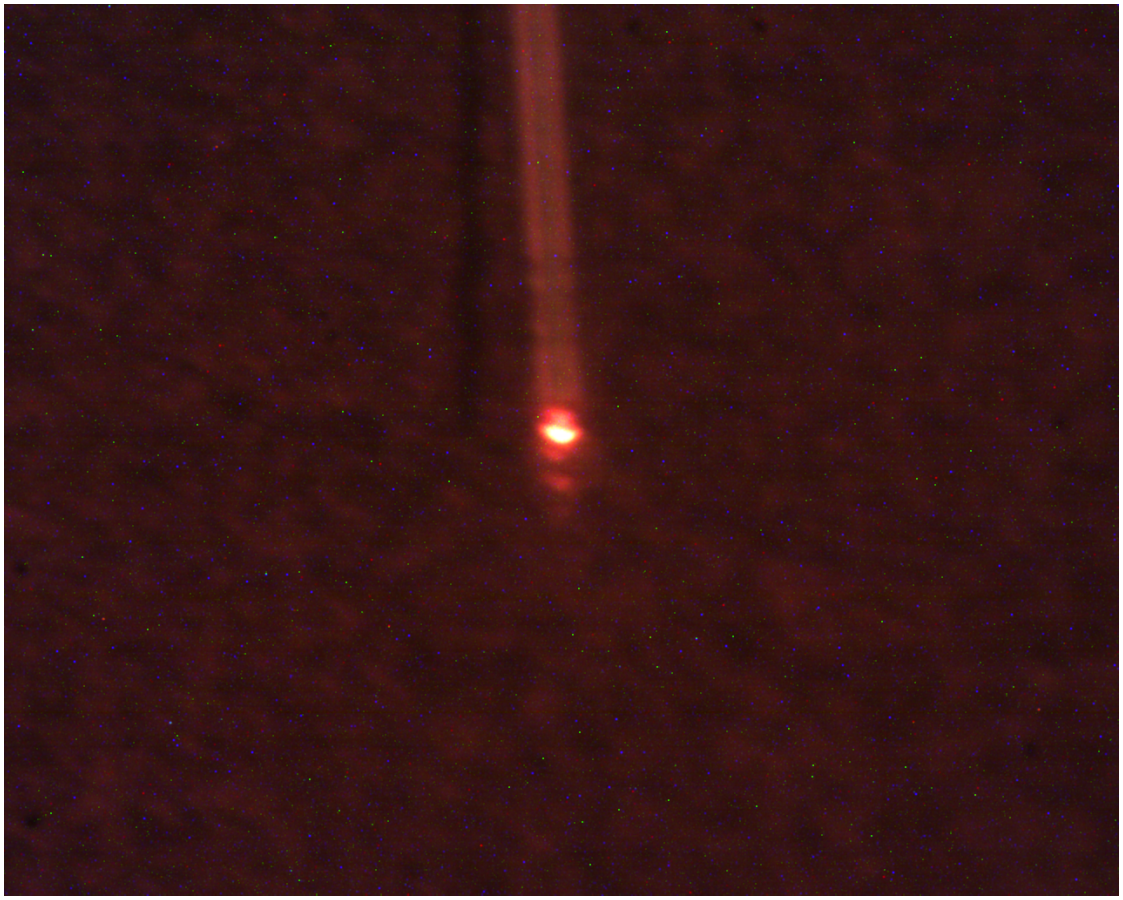

Figure 5.3: shows a broad-spectrum 488nm light source transmitted through a low-stress nitride Needle. The 488nm source looks mostly greenish but it includes wavelengths from blue to red. The tip looks mostly red because the nitride absorbs much less of the red light than the blue light. This is likely due to the low-stress nitride being more silicon rich than standard silicon nitride.

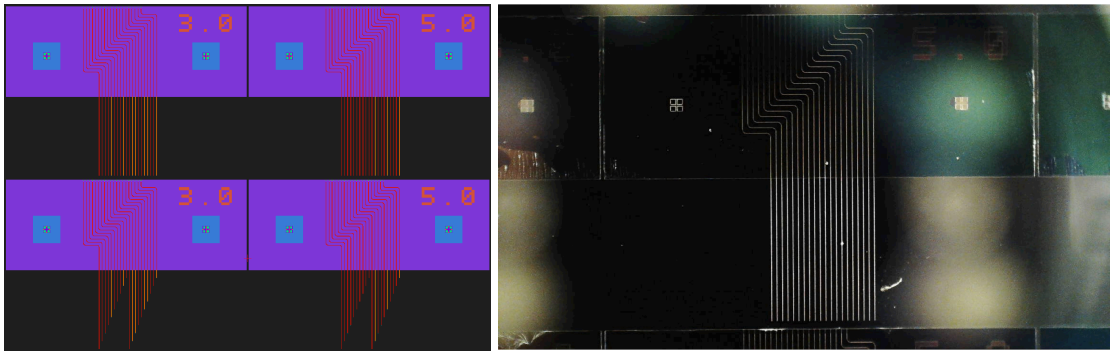

Figure 5.4: Left is a sampling from the CAD for the contact photolithography mask layers showing the 3 and 5 μm sets needles. Some chips have needles with all equivalent lengths and some chips have varied lengths. Right is a photograph of one chip set of fabricated silicon nitride probes.

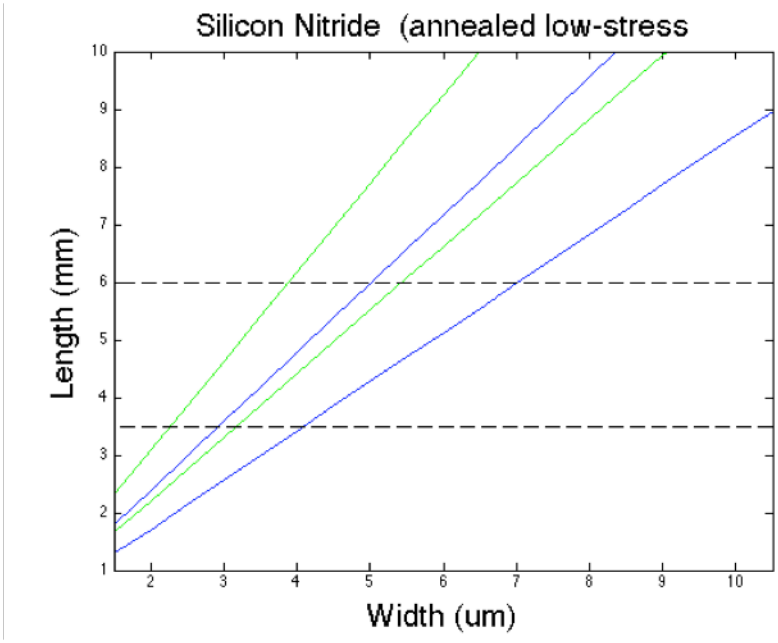

Figure 5.5: Length versus width graph is a similar graph to Figure 2.4 for silicon, but for the low-stress nitride recipe in this chapter instead. It shows the critical dimensions before buckling for the needles to penetrate mouse brain with dura in tact. The green lines bound the region corresponding to a pointed tip and the blue lines bound the region corresponding to a curved tip. The upper lines of both regions correspond to fixed/fixed boundary conditions and the lower lines of both regions correspond to fixed/pinned boundary conditions.

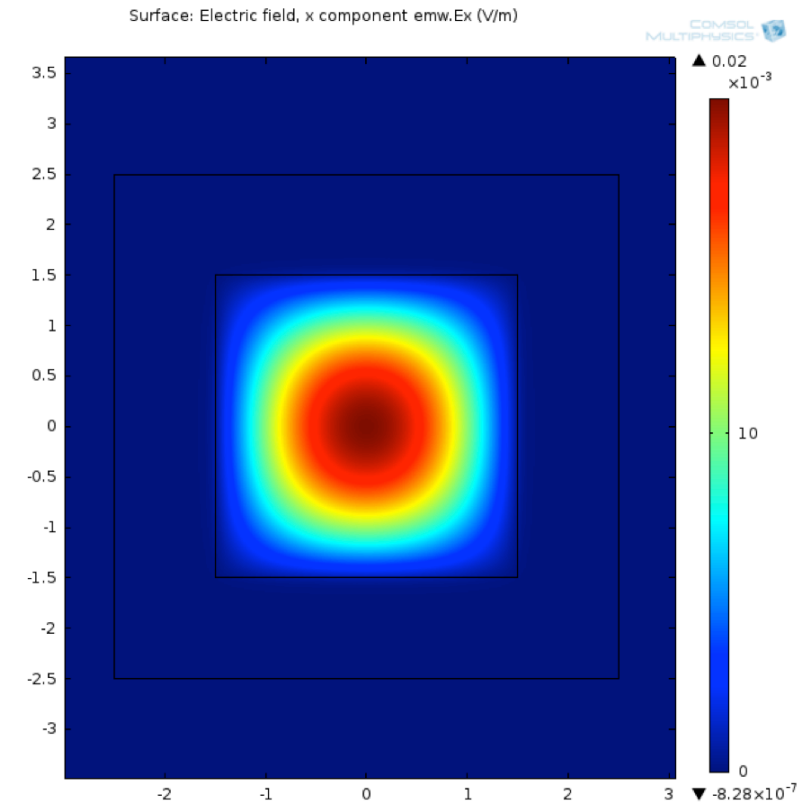

Figure 5.6: The Comsol simulated optical mode of a 3 x 3µm cross-section needle and an effective index of n = 2.27.

APPENDIX

A1. Python code for measuring a series of spectral components with a spectrum analyzer (used specifically with an Agilent E4407B):

```
###!/usr/bin/python

# -*- coding: utf-8 -*-
"""
Created on 30 Apr 2017

multiscan code for measuring a series of narrow peaks, spaced relatively far apart by
Romy Fain

adapted from code by Avik Dutt for single scan
"""

import numpy as np
import pyvisa, matplotlib
matplotlib.rcParams['backend.qt4'] = 'PySide'
import PySide
import pylab as p
import time
import glob
import matplotlib.pyplot as plt

plt.close("all")
rm = pyvisa.ResourceManager()
print rm.list_resources()
rf = rm.open_resource(u'GPIB0::18::INSTR')
print(rf.query('*IDN?'))
rf.write(':INITiate:CONTinuous ON')       #continuous mode sweep
#rf.write(':INITiate:CONTinuous OFF')       #single mode sweep

fundFreq = 80.05
freq = [1600.98]

###%% Span
span = '10KHZ'
rf.write(':FREQuency:SPAN '+span)
```

```
#%% #Set RBW
RBW = '100HZ'
rf.write(':BANDwidth:RESolution '+RBW)

#%% #Set VBW
VBW = '100HZ'
rf.write(':BANDwidth:VIDeo '+VBW)

#%% Ref level
ref_l = '-80DBM'#-120
rf.write(':DISPlay:WINDow:TRACe:Y:SCALe:RLEVel ' + ref_l)

#%% Sweep time
sweep_time = 'AUTO'
rf.write(':SWEep:TIME:AUTO ON')

#%% Y axis scale per div
y_scale = "7"
rf.write(':DISPlay:WINDow:TRACe:Y:SCALe:PDIVision ' + y_scale)

#%% ST= sweeptime[ms]
ST = rf.query_ascii_values(':SWEep:TIME?')

#%% Average
aveN = '40'

peakFreq = []
stdevPeak = []
peakAmp = []
i = 0

while(freq[i]<2250):
    data = []
    aveData = []

    ##%% center freq
    center_f = str(freq[i]) + 'MHZ'
    rf.write(':FREQuency:CENTer '+center_f)

    #%% Read data
    for q in range (aveN):
        time.sleep(2*ST[0])
        data.append(np.array(rf.query_ascii_values('TRACe? TRACE1')))
        #Get start and stop frequencies
        N = len(data[q])
        start_f = rf.query_ascii_values(':FREQuency:STARt?')[0]
```

```
        stop_f = rf.query_ascii_values(':FREQuency:STOP?')[0]
        freqs = np.linspace(start_f, stop_f, N)

        plotting = 1
        plt.figure()
        if plotting:
            p.plot(freqs/1.e6, data[q])
            p.xlabel('Frequency (MHz)')
            p.ylabel('Amplitude (dBm)')
            p.title(str(freq[i])+'MHz'+'_'+str(q))

        f =
r"spect"+str(q)+"_ctrF"+center_f+"_span"+span+"_RBW"+RBW+"_VBW"+VBW+"_s
weepTime"+sweep_time+"_refLevel"+ref_l+"_yScale"+y_scale+".txt"

        save_dir = "C:\\Users\\romyfain\\Desktop\\spectrumAnalyzerCode\\speedData\\"

        data_to_write = np.array([freqs.T,data[q].T]).T
        np.savetxt(save_dir+f, data_to_write, delimiter='\t')

############
    aveData = sum(data,0)/(q+1)
    stdevData = np.std(data,0)

    peakAmp.append(max(aveData))

    peakFreq.append(freq[i]-0.005+((0.01/N)*np.argmax(aveData)))
    stdevPeak.append(stdevData[np.argmax(aveData)])

    freq.append((freq[i]-0.005+((0.01/N)*np.argmax(aveData))) + fundFreq)

############
    plt.figure()
    plotting = 1
    if plotting:
        p.plot(freqs/1.e6, aveData)
        p.xlabel('Frequency (MHz)')
        p.ylabel('Amplitude (dBm)')
        p.title('Average over 40 scans: '+ str(freq[i])+'MHz')

        graph_filename=
str(peakFreq[i])+"MHz_"+str(peakAmp[i])+"dBm_PEAKS_span"+span+"_RBW"+RB
W+"_VBW"+VBW+"_sweepTime"+sweep_time+"_refLevel"+ref_l+"_yScale"+y_scal
e+".png"
```

```
graph_path="C:\\Users\\romyfain\\Desktop\\spectrumAnalyzerCode\\speedData\\peaks\\
graphs\\"
        p.savefig(graph_path+graph_filename)

    i+= 1
    plt.close("all")

f_peaks =
"PEAKS_span"+span+"_RBW"+RBW+"_VBW"+VBW+"_sweepTime"+sweep_time+"
_refLevel"+ref_l+"_yScale"+y_scale+".txt"

save_dir = "C:\\Users\\romyfain\\Desktop\\spectrumAnalyzerCode\\speedData\\peaks\\"

to_write_peaks =
np.array([np.array(peakFreq).T,np.array(peakAmp).T,np.array(stdevPeak).T]).T
np.savetxt(save_dir+f_peaks, to_write_peaks, delimiter='\t')
```

A2. List of a Some Strong Spectral Lines from 3 to 6 μm

chemical species	wavelength (μm)	absorption(cm^2/molecule)
Acetylene	2.964. 3.04	1E-18
Ammonia	8.5 to 12	3E-18
	2.85 to 3.15(2.997,2.904)	1.2E-19
	2.2 to 2.35	3E-20
Benzene	14.7	1E-17
	~3.5	1E-21
Butane	~3.5	8.5E-19
	~2.5	5E-21
Butanol	~3.5	5E-19
	~2.7	5E-20
Butene	3.2-3.6	3E-19
Carbon dioxide	4.2-4.34	1.3E-17
Carbon monoxide	4.5-4.9	2E-18
Cyclohexane	~3.5	4E-18
Ethane	3.35	2E-18
Formaldehyde	5.73	1.5E-18
	3.6	1E-18
Carbonyl sulfide	4.85	6E-18
Chlorosulfonyl isocyanate	4.431	6.5E-18
Cyclopropane	3.292	1.5E-18
Ethanol	~3.5	2.5E-19
	2.8	9E-20
Ethylene	~10.5	2E-18
	2.2	1.6E-20
Hydrazine	3	3E-20
Hydrogen cyanide	2.5	1.2E-19
Hydrogen fluoride	2.4-2.5	7E-18
Hydrogen sulfide	2.55-2.75	8E-21
Hydroxyl radical	2.8	8E-20
Methanol	9.5	1E-18
	2.72	1E-19
methane	3.312	1.5E-18
Methyl chloride	2.2	2E-20
Methyl fluoride	2.25	2E-20
Nitric acid	2.815	8E-19
Nitric oxide	2.67	1E-20
Nitrous oxide	2.86	1.2E-19
Phosphine	2.925	2.5E-20

Propane	3.359	1.15E-18
Water	6.27	9E-19
	2.734	7.5E-19
	2.662	7E-19
Xenon	3.508	

REFERENCES

1. E. Rephaeli, A. Raman, and S. Fan, "Ultrabroadband Photonic Structures To Achieve High-Performance Daytime Radiative Cooling," Nano Lett. 130311121615001 (2013).
2. Y. Cui, K. H. Fung, J. Xu, H. Ma, Y. Jin, S. He, and N. X. Fang, "Ultrabroadband Light Absorption by a Sawtooth Anisotropic Metamaterial Slab," Nano Lett. **12**, 1443–1447 (2012).
3. N. G. Horton, K. Wang, D. Kobat, C. G. Clark, F. W. Wise, C. B. Schaffer, and C. Xu, "In vivo three-photon microscopy of subcortical structures within an intact mouse brain," Nat. Photonics **7**, 205–209 (2013).
4. D. Kobat, N. G. Horton, and C. Xu, "In vivo two-photon microscopy to 1.6-mm depth in mouse cortex," J. Biomed. Opt. **16**, 106014–106014 (2011).
5. L. Shi, L. A. Sordillo, A. Rodríguez-Contreras, and R. Alfano, "Transmission in near-infrared optical windows for deep brain imaging," J. Biophotonics **9**, 38–43 (2016).
6. E. Thimsen, B. Sadtler, and M. Y. Berezin, "Shortwave-infrared (SWIR) emitters for biological imaging: a review of challenges and opportunities," Nanophotonics **0**, (2017).
7. P. A. West, M. P. G. Bostrom, P. A. Torzilli, and N. P. Camacho, "Fourier transform infrared spectral analysis of degenerative cartilage: an infrared fiber optic probe and imaging study," Appl. Spectrosc. **58**, 376–381 (2004).

8. X. Ji, B. Zhang, M. Krishnamurthi, J. Badding, and V. Gopalan, "Mid-infrared spectroscopic imaging enabled by an array of Ge-filled waveguides in a microstructured optical fiber probe," Opt. Express **22**, 28459 (2014).

9. U. Bindig, H. Winter, W. Wa, K. Zelianeos, G. Mu, and others, "Fiber-optical and microscopic detection of malignant tissue by use of infrared spectrometry," J. Biomed. Opt. **7**, 100–108 (2002).

10. B. Mizaikoff, "Waveguide-enhanced mid-infrared chem/bio sensors," Chem. Soc. Rev. **42**, 8683 (2013).

11. B. Kateb, V. Yamamoto, C. Yu, W. Grundfest, and J. P. Gruen, "Infrared thermal imaging: A review of the literature and case report," NeuroImage **47**, T154–T162 (2009).

12. E. P. Popov and T. A. Balan, *Engineering Mechanics of Solids*, 2nd ed (Prentice Hall, 1998).

13. W. F. Hosford, *Materials for Engineers* (Cambridge University Press, 2008).

14. A. F. Bower, *Applied Mechanics of Solids* (CRC Press, 2010).

15. C. R. Pollack and M. Lipson, *Integrated Photonics* (Kluwer Academic Publishers, 2003).

16. E. Hecht, *Optics*, 4th ed (Addison-Wesley, 2002).

17. I. P. Kaminow and L. W. Stulz, "Loss in cleaved Ti-diffused LiNbO3 waveguides," Appl. Phys. Lett. **33**, 62–64 (1978).

18. R. Regener and W. Sohler, "Loss in low-finesse Ti: LiNbO3 optical waveguide resonators," Appl. Phys. B **36**, 143–147 (1985).

19. K. H. Park, M. W. Kim, Y. T. Byun, D. Woo, S. H. Kim, S. S. Choi, Y. Chung, W. R. Cho, S. H. Park, and U. Kim, "Nondestructive propagation loss and facet reflectance measurements of GaAs/AlGaAs strip-loaded waveguides," J. Appl. Phys. **78**, 6318 (1995).

20. A. De Rossi, V. Ortiz, M. Calligaro, L. Lanco, S. Ducci, V. Berger, and I. Sagnes, "Measuring propagation loss in a multimode semiconductor waveguide," J. Appl. Phys. **97**, 73105 (2005).

21. S. Taebi, M. Khorasaninejad, and S. S. Saini, "Modified Fabry-Perot interferometric method for waveguide loss measurement," Appl. Opt. **47**, 6625–6630 (2008).

22. A. H. Nejadmalayeri, F. N. C. Wong, T. D. Roberts, P. Battle, and F. X. Kärtner, "Guided wave optics in periodically poled KTP: quadratic nonlinearity and prospects for attosecond jitter characterization," Opt. Lett. **34**, 2522 (2009).

23. R. Waldhäusl, B. Schnabel, P. Dannberg, E.-B. Kley, A. Bräuer, and W. Karthe, "Efficient Coupling into Polymer Waveguides by Gratings," Appl. Opt. **36**, 9383–9390 (1997).

24. A. Oppenheim, A. Willsky, and S. Hamid, *Signals and Systems (2nd Edition)* (Prentice Hall, 1996).

25. R. R. Grote, B. Souhan, N. Ophir, J. B. Driscoll, K. Bergman, H. Bahkru, W. M. J. Green, and R. M. Osgood, "Extrinsic photodiodes for integrated mid-infrared silicon photonics," Optica **1**, 264 (2014).

26. S. M. Sze, *Physics of Semiconductor Devices.* (John Wiley & Sons, 2006).

27. J. P. Prineas, J. Yager, S. Seyedmohamadi, and J. T. Olesberg, "Leakage mechanisms and potential performance of molecular-beam epitaxially grown GaInAsSb 2.4 μm photodiode detectors," J. Appl. Phys. **103**, 104511 (2008).

28. P. Theer and W. Denk, "On the fundamental imaging-depth limit in two-photon microscopy," JOSA A **23**, 3139–3149 (2006).

29. A. N. Zorzos, E. S. Boyden, and C. G. Fonstad, "Multiwaveguide implantable probe for light delivery to sets of distributed brain targets," Opt. Lett. **35**, 4133–4135 (2010).

30. E. Stark, T. Koos, and G. Buzsaki, "Diode probes for spatiotemporal optical control of multiple neurons in freely moving animals," J. Neurophysiol. **108**, 349–363 (2012).

31. F. Wu, E. Stark, M. Im, I.-J. Cho, E.-S. Yoon, G. Buzsáki, K. D. Wise, and E. Yoon, "An implantable neural probe with monolithically integrated dielectric waveguide and recording electrodes for optogenetics applications," J. Neural Eng. **10**, 56012 (2013).

32. E. Shim, Y. Chen, S. Masmanidis, and M. Li, "Multisite silicon neural probes with integrated silicon nitride waveguides and gratings for optogenetic applications," Sci. Rep. **6**, 22693 (2016).

33. K. D. Wise, J. B. Angell, and A. Starr, "An Integrated-Circuit Approach to Extracellular Microelectrodes," Biomed. Eng. IEEE Trans. Bio-Med. Eng. **3**, 238–247 (1970).

34. S. K. Masmanidis, J. Du, M. L. Roukes, and G. J. Laurent, *Micromachined Neural Probes* (Google Patents, 2013).

35. R. P. J. Barretto, B. Messerschmidt, and M. J. Schnitzer, "In vivo fluorescence imaging with high-resolution microlenses," Nat. Methods **6**, 511–512 (2009).

36. L. V. Doronina-Amitonova, I. V. Fedotov, O. I. Ivashkina, M. A. Zots, A. B. Fedotov, K. V. Anokhin, and A. M. Zheltikov, "Implantable fiber-optic interface for parallel multisite long-term optical dynamic brain interrogation in freely moving mice," Sci. Rep. **3**, (2013).

37. N. Farah, A. Levinsky, I. Brosh, I. Kahn, and S. Shoham, "Holographic fiber bundle system for patterned optogenetic activation of large-scale neuronal networks," Neurophotonics **2**, 45002–45002 (2015).

38. C. J. Davey, A. Argyros, S. C. Fleming, and S. G. Solomon, "Multimodal optogenetic neural interfacing device fabricated by scalable optical fiber drawing technique," Appl. Opt. **54**, 10068 (2015).

39. R. A. McLaughlin, B. C. Quirk, A. Curatolo, R. W. Kirk, L. Scolaro, D. Lorenser, P. D. Robbins, B. A. Wood, C. M. Saunders, and D. D. Sampson, "Imaging of Breast Cancer With Optical Coherence Tomography Needle Probes: Feasibility and Initial Results," IEEE J. Sel. Top. Quantum Electron. **18**, 1184–1191 (2012).

40. P. Anikeeva, A. S. Andalman, I. Witten, M. Warden, I. Goshen, L. Grosenick, L. A. Gunaydin, L. M. Frank, and K. Deisseroth, "Optetrode: a multichannel readout for optogenetic control in freely moving mice," Nat. Neurosci. **15**, 163–170 (2011).

41. T. V. F. Abaya, S. Blair, P. Tathireddy, L. Rieth, and F. Solzbacher, "A 3D glass optrode array for optical neural stimulation," Biomed. Opt. Express **3**, 3087–3104 (2012).

42. F. Pisanello, L. Sileo, I. A. Oldenburg, M. Pisanello, L. Martiradonna, J. A. Assad, B. L. Sabatini, and M. De Vittorio, "Multipoint-Emitting Optical Fibers for Spatially Addressable In Vivo Optogenetics," Neuron **82**, 1245–1254 (2014).

43. A. Canales, X. Jia, U. P. Froriep, R. A. Koppes, C. M. Tringides, J. Selvidge, C. Lu, C. Hou, L. Wei, Y. Fink, and P. Anikeeva, "Multifunctional fibers for simultaneous optical, electrical and chemical interrogation of neural circuits in vivo," Nat. Biotechnol. **33**, 277–284 (2015).

44. J. Lee, I. Ozden, Y.-K. Song, and A. V. Nurmikko, "Transparent intracortical microprobe array for simultaneous spatiotemporal optical stimulation and multichannel electrical recording," Nat. Methods **12**, 1157–1162 (2015).

45. D. J. Edel, V. V. Toi, V. M. McNeil, and L. D. Clark, "Factors influencing the biocompatibility of insertable silicon microshafts in cerebral cortex," Biomed. Eng. IEEE Trans. On **39**, 635–643 (1992).

46. D. H. Szarowski, M. D. Andersen, S. Retterer, A. J. Spence, M. Isaacson, H. G. Craighead, J. N. Turner, and W. Shain, "Brain responses to micro-machined silicon devices," Brain Res. **983**, 23–35 (2003).

47. R. Biran, D. C. Martin, and P. A. Tresco, "Neuronal cell loss accompanies the brain tissue response to chronically implanted silicon microelectrode arrays," Exp. Neurol. **195**, 115–126 (2005).

48. J. C. Williams, J. A. Hippensteel, J. Dilgen, W. Shain, and D. R. Kipke, "Complex impedance spectroscopy for monitoring tissue responses to inserted neural implants," J. Neural Eng. **4**, 410–423 (2007).

49. M. J. Farrar, F. W. Wise, J. R. Fetcho, and C. B. Schaffer, "In Vivo Imaging of Myelin in the Vertebrate Central Nervous System Using Third Harmonic Generation Microscopy," Biophys. J. **100**, 1362–1371 (2011).

50. N. Ji, T. R. Sato, and E. Betzig, "Characterization and adaptive optical correction of aberrations during in vivo imaging in the mouse cortex," Proc. Natl. Acad. Sci. **109**, 22–27 (2012).

51. P. Mahou, M. Zimmerley, K. Loulier, K. S. Matho, G. Labroille, X. Morin, W. Supatto, J. Livet, D. Débarre, and E. Beaurepaire, "Multicolor two-photon tissue imaging by wavelength mixing," Nat. Methods **9**, 815–818 (2012).

52. S. S. Howard, A. Straub, N. G. Horton, D. Kobat, and C. Xu, "Frequency-multiplexed in vivo multiphoton phosphorescence lifetime microscopy," Nat. Photonics **7**, 33–37 (2012).

53. N. G. Horton, K. Wang, D. Kobat, C. G. Clark, F. W. Wise, C. B. Schaffer, and C. Xu, "In vivo three-photon microscopy of subcortical structures within an intact mouse brain," Nat. Photonics **7**, 205–209 (2013).

54. T.-H. Tsai, C.-Y. Lin, H.-J. Tsai, S.-Y. Chen, S.-P. Tai, K.-H. Lin, and C.-K. Sun, "Biomolecular imaging based on far-red fluorescent protein with a high two-photon excitation action cross section," Opt. Lett. **31**, 930–932 (2006).

55. J. Du, M. L. Roukes, and S. C. Masmanidis, "Dual-side and three-dimensional microelectrode arrays fabricated from ultra-thin silicon substrates," J. Micromechanics Microengineering **19**, 75008 (2009).

56. A. Ramkumar, A. Lal, D. A. Paduch, and P. N. Schlegel, "An Ultrasonically Actuated Silicon-Microprobe-Based Testicular Tubule Assay," IEEE Trans. Biomed. Eng. **56**, 2666–2674 (2009).

57. A. N. Zorzos, E. S. Boyden, and C. G. Fonstad, "Multiwaveguide implantable probe for light delivery to sets of distributed brain targets," Opt. Lett. **35**, 4133 (2010).

58. J. Du, T. J. Blanche, R. R. Harrison, H. A. Lester, and S. C. Masmanidis, "Multiplexed, High Density Electrophysiology with Nanofabricated Neural Probes," PLoS ONE **6**, e26204 (2011).

59. P.-C. Chen, C. G. Clark, C. Schaffer, R. F. Gilmour, and A. Lal, "Ultrasonically enabled neural probes with co-located electrical and mechanical transduction," in (IEEE, 2012), pp. 350–353.

60. F. Wu, E. Stark, M. Im, I.-J. Cho, E.-S. Yoon, G. Buzsáki, K. D. Wise, and E. Yoon, "An implantable neural probe with monolithically integrated dielectric waveguide and recording electrodes for optogenetics applications," J. Neural Eng. **10**, 56012 (2013).

61. K. Najafi, J. Ji, and K. D. Wise, "Scaling limitations of silicon multichannel recording probes," IEEE Trans. Biomed. Eng. **37**, 1–11 (1990).

62. J. Yang, T. Ono, and M. Esashi, "Mechanical behavior of ultrathin microcantilever," Sens. Actuators Phys. **82**, 102–107 (2000).

63. S. J. Oh, J. K. Song, J. W. Kim, and S. J. Kim, "A High-Yield Fabrication Process for Silicon Neural Probes," IEEE Trans. Biomed. Eng. **53**, 351–354 (2006).

64. B. A. Bryce, B. Robert Ilic, M. C. Reuter, and S. Tiwari, "Silicon nanowire atomic force microscopy probes for high aspect ratio geometries," Appl. Phys. Lett. **100**, 213106 (2012).

65. V. Normand, D. L. Lootens, E. Amici, K. P. Plucknett, and P. Aymard, "New Insight into Agarose Gel Mechanical Properties," Biomacromolecules **1**, 730–738 (2000).

66. Q. Chen, B. Suki, and K.-N. An, "Dynamic Mechanical Properties of Agarose Gels Modeled by a Fractional Derivative Model," J. Biomech. Eng. **126**, 666 (2004).

67. A. A. Sharp, A. M. Ortega, D. Restrepo, D. Curran-Everett, and K. Gall, "In Vivo Penetration Mechanics and Mechanical Properties of Mouse Brain Tissue at Micrometer Scales," IEEE Trans. Biomed. Eng. **56**, 45–53 (2009).

68. P.-C. Chen, C. Clark, C.-P. J. Shen, C. Schaffer, and A. Lal, "Ultrasonically actuated inserted neural probes for increased recording reliability," in *Solid-State Sensors, Actuators and Microsystems (TRANSDUCERS & EUROSENSORS XXVII), 2013 Transducers & Eurosensors XXVII: The 17th International Conference on* (IEEE, 2013), pp. 872–875.

69. R. R. Llinás, K. D. Walton, M. Nakao, I. Hunter, and P. A. Anquetil, "Neuro-vascular central nervous recording/stimulating system: Using nanotechnology probes," J. Nanoparticle Res. **7**, 111–127 (2005).

70. W. J. Bae, B. P. Ruddy, A. G. Richardson, I. W. Hunter, and E. Bizzi, "Cortical recording with polypyrrole microwire electrodes," in *Engineering in Medicine and*

Biology Society, 2008. EMBS 2008. 30th Annual International Conference of the IEEE (IEEE, 2008), pp. 5794–5797.

71. G. Guitchounts, J. E. Markowitz, W. A. Liberti, and T. J. Gardner, "A carbon-fiber electrode array for long-term neural recording," J. Neural Eng. **10**, 46016 (2013).

72. Z. Han, V. Singh, D. Kita, C. Monmeyran, P. Becla, P. Su, J. Li, X. Huang, L. C. Kimerling, J. Hu, K. Richardson, D. T. H. Tan, and A. Agarwal, "On-chip chalcogenide glass waveguide-integrated mid-infrared PbTe detectors," Appl. Phys. Lett. **109**, 71111 (2016).

73. A. Rogalski, "HgCdTe infrared detector material: history, status and outlook," Rep. Prog. Phys. **68**, 2267–2336 (2005).

74. J. Qiu, B. Weng, Z. Yuan, and Z. Shi, "Study of sensitization process on mid-infrared uncooled PbSe photoconductive detectors leads to high detectivity," J. Appl. Phys. **113**, 103102 (2013).

75. S. Keuleyan, E. Lhuillier, V. Brajuskovic, and P. Guyot-Sionnest, "Mid-infrared HgTe colloidal quantum dot photodetectors," Nat. Photonics **5**, 489–493 (2011).

76. K. W. Berryman, S. A. Lyon, and M. Segev, "Mid-infrared photoconductivity in InAs quantum dots," Appl. Phys. Lett. **70**, 1861–1863 (1997).

77. B. J. Frey, D. B. Leviton, and T. J. Madison, "Temperature-dependent refractive index of silicon and germanium," in *SPIE Astronomical Telescopes+ Instrumentation* (International Society for Optics and Photonics, 2006), p. 62732J–62732J.

78. G. Z. Mashanovich, G. T. Reed, M. Nedeljkovic, J. Soler Penades, C. J. Mitchell, A. Z. Khokhar, C. J. Littlejohns, S. Stankovic, X. Chen, L. Shen, N. Healy, A. C.

Peacock, C. Alonso-Ramos, A. Ortega-Monux, G. Wanguemert-Perez, I. Molina-Fernandez, P. Cheben, J. J. Ackert, A. P. Knights, F. Y. Gardes, and D. J. Thomson, "Silicon and germanium mid-infrared photonics," in M. Razeghi, ed. (2016), p. 97550W.

79. N. Sclar, "Properties of doped silicon and germanium infrared detectors," Prog. Quantum Electron. **9**, 149–257 (1984).

80. F. H. L. Koppens, T. Mueller, P. Avouris, A. C. Ferrari, M. S. Vitiello, and M. Polini, "Photodetectors based on graphene, other two-dimensional materials and hybrid systems," Nat. Nanotechnol. **9**, 780–793 (2014).

81. C.-H. Liu, Y.-C. Chang, T. B. Norris, and Z. Zhong, "Graphene photodetectors with ultra-broadband and high responsivity at room temperature," Nat. Nanotechnol. **9**, 273–278 (2014).

82. Y. Yao, R. Shankar, P. Rauter, Y. Song, J. Kong, M. Loncar, and F. Capasso, "High-Responsivity Mid-Infrared Graphene Detectors with Antenna-Enhanced Photocarrier Generation and Collection," Nano Lett. **14**, 3749–3754 (2014).

83. S. M. Geyer, J. M. Scherer, F. B. Jaworski, and M. G. Bawendi, "Multispectral imaging via luminescent down-shifting with colloidal quantum dots," Opt. Mater. Express **3**, 1167 (2013).

84. Z. Huang, J. E. Carey, M. Liu, X. Guo, E. Mazur, and J. C. Campbell, "Microstructured silicon photodetector," Appl. Phys. Lett. **89**, 33506 (2006).

85. D. J. Thomson, L. Shen, J. J. Ackert, E. Huante-Ceron, A. P. Knights, M. Nedeljkovic, A. C. Peacock, and G. Z. Mashanovich, "Optical detection and modulation at 2μm-25μm in silicon," Opt. Express **22**, 10825 (2014).

86. B. Souhan, R. R. Grote, C. P. Chen, H.-C. Huang, J. B. Driscoll, M. Lu, A. Stein, H. Bakhru, K. Bergman, W. M. J. Green, and R. M. Osgood, "Si^+-implanted Si-wire waveguide photodetectors for the mid-infrared," Opt. Express **22**, 27415 (2014).

87. J. J. Ackert, D. J. Thomson, L. Shen, A. C. Peacock, P. E. Jessop, G. T. Reed, G. Z. Mashanovich, and A. P. Knights, "High-speed detection at two micrometres with monolithic silicon photodiodes," Nat. Photonics **9**, 393–396 (2015).

88. B. Souhan, C. Chen, M. Lu, A. Stein, H. Bakhru, R. Grote, K. Bergman, W. Green, and R. Osgood, "Ar+-Implanted Si-Waveguide Photodiodes for Mid-Infrared Detection," Photonics **3**, 46 (2016).

89. C. R. Petersen, U. Møller, I. Kubat, B. Zhou, S. Dupont, J. Ramsay, T. Benson, S. Sujecki, N. Abdel-Moneim, Z. Tang, D. Furniss, A. Seddon, and O. Bang, "Mid-infrared supercontinuum covering the 1.4–13.3 μm molecular fingerprint region using ultra-high NA chalcogenide step-index fibre," Nat. Photonics **8**, 830–834 (2014).

90. L. S. Rothman, I. E. Gordon, Y. Babikov, A. Barbe, D. Chris Benner, P. F. Bernath, M. Birk, L. Bizzocchi, V. Boudon, L. R. Brown, A. Campargue, K. Chance, E. A. Cohen, L. H. Coudert, V. M. Devi, B. J. Drouin, A. Fayt, J.-M. Flaud, R. R. Gamache, J. J. Harrison, J.-M. Hartmann, C. Hill, J. T. Hodges, D. Jacquemart, A. Jolly, J. Lamouroux, R. J. Le Roy, G. Li, D. A. Long, O. M. Lyulin, C. J. Mackie, S. T. Massie, S. Mikhailenko, H. S. P. M?ller, O. V. Naumenko, A. V. Nikitin, J. Orphal, V. Perevalov, A. Perrin, E. R. Polovtseva, C. Richard, M. A. H. Smith, E. Starikova, K. Sung, S. Tashkun, J. Tennyson, G. C. Toon, V. G.

Tyuterev, and G. Wagner, "The HITRAN2012 molecular spectroscopic database," J. Quant. Spectrosc. Radiat. Transf. **130**, 4–50 (2013).

91. P. Migliorato and C. T. Elliott, "Sulphur doped silicon IR detectors," Solid-State Electron. **21**, 443–447 (1978).

92. R. R. Grote, B. Souhan, N. Ophir, J. B. Driscoll, K. Bergman, H. Bahkru, W. M. J. Green, and R. M. Osgood, "Extrinsic photodiodes for integrated mid-infrared silicon photonics," Optica **1**, 264 (2014).

93. N. Sclar, "Extrinsic silicon detectors for 3–5 and 8–14 μm," Infrared Phys. **16**, 435–448 (1976).

94. S. D. Brotherton, M. J. King, and G. J. Parker, "The electrical properties of sulphur in silicon," J. Appl. Phys. **52**, 4649–4658 (1981).

95. H. Jiang and C. Chen, "Analysis and Calculation of Electronic Properties and Light Absorption of Defective Sulfur-Doped Silicon and Theoretical Photoelectric Conversion Efficiency," J. Phys. Chem. A **119**, 3753–3761 (2015).

96. I. Umezu, J. M. Warrender, S. Charnvanichborikarn, A. Kohno, J. S. Williams, M. Tabbal, D. G. Papazoglou, X.-C. Zhang, and M. J. Aziz, "Emergence of very broad infrared absorption band by hyperdoping of silicon with chalcogens," J. Appl. Phys. **113**, 213501 (2013).

97. D. Recht, M. J. Smith, S. Charnvanichborikarn, J. T. Sullivan, M. T. Winkler, J. Mathews, J. M. Warrender, T. Buonassisi, J. S. Williams, S. Gradečak, and M. J. Aziz, "Supersaturating silicon with transition metals by ion implantation and pulsed laser melting," J. Appl. Phys. **114**, 124903 (2013).

98. J. P. Mailoa, A. J. Akey, C. B. Simmons, D. Hutchinson, J. Mathews, J. T. Sullivan, D. Recht, M. T. Winkler, J. S. Williams, J. M. Warrender, P. D. Persans, M. J. Aziz, and T. Buonassisi, "Room-temperature sub-band gap optoelectronic response of hyperdoped silicon," Nat. Commun. **5**, (2014).

99. T. G. Kim, J. M. Warrender, and M. J. Aziz, "Strong sub-band-gap infrared absorption in silicon supersaturated with sulfur," Appl. Phys. Lett. **88**, 241902 (2006).

100. A. G. Griffith, R. K. W. Lau, J. Cardenas, Y. Okawachi, A. Mohanty, R. Fain, Y. H. D. Lee, M. Yu, C. T. Phare, C. B. Poitras, A. L. Gaeta, and M. Lipson, "Silicon-chip mid-infrared frequency comb generation," Nat. Commun. **6**, 6299 (2015).

101. M. Lishchynska, N. Cordero, O. Slattery, and C. O'Mahony, "Spring Constant Models for Analysis and Design of MEMS Plates on Straight or Meander Tethers," Sens. Lett. **4**, 200–205 (2006).

102. R. Grote, *Nanophotonics for Optoelectronic Devices: Extrinsic Silicon Photonic Receivers and Organic Photovoltaics* (Columbia University, 2014).

103. A. Bagolini, A. Picciotto, M. Crivellari, P. Conci, and P. Bellutti, "PECVD silicon-rich nitride and low stress nitride films mechanical characterization using membrane point load deflection," J. Micromechanics Microengineering **26**, 25004 (2016).